

Joseph Cook  
IBERS, Aberystwyth University  
[joc102@aber.ac.uk](mailto:joc102@aber.ac.uk)  
26/09/2019

**re: Cook et al. 2019: Glacier algae accelerate melt rates on the south-western Greenland Ice Sheet  
Authors response to reviewer comments, round 2.**

Dear editor and reviewers,

we are very grateful for the second set of reviews of our paper. We have endeavoured to address all the comments made by both reviewers to the best of our ability. Most notably, we have removed the DISORT inversion from our study entirely, as Reviewer 1 pointed out strange behaviour at the short visible wavelengths that we could not resolve. This has been replaced by an alternative method that uses measured particle size distributions and mineral mass-fractions from field data along with mineral refractive indices from the past literature to estimate optical properties from the local dusts.

In this document, we provide point-by-point responses to the reviewer comments and a copy of the manuscript with the main changes highlighted. We have also submitted a revised manuscript and substantial new supplementary information as well as updating our data and code repositories (we highlight to the editor that we have held back from minting doi's for these repositories until the end of the peer-review process so that we can update according to reviewer queries).

We sincerely thank the reviewers for their time and effort in reviewing this paper. We consider the paper to be much better as a result and we hope that this manuscript satisfies the concerns raised in the comments.

Kind regards,

Joseph Cook and co-authors

**Second review of Cook et al. for TCD, August 2019, by Stephen Warren  
“Glacier algae accelerate melt rates on the south-western Greenland Ice Sheet”**

**Recommendation: Major revision required.**

This paper is still not ready for publication. Concerning the melting ice surface of the West- Greenland ablation zone in summer, the authors argue that addition of dust causes the ice albedo to increase, so that any reduction of ice albedo by light-absorbing impurities would be due to algae. This denial of a role for dust in reducing albedo is based on several questionable arguments, which I will point out in this review. Most of these questionable arguments can be classified into one of three classes of disconnects: (a) The authors’ response to my review, saying how the paper was changed, does not correspond with what the revised paper actually shows. (b) The way figures are described in the text does not correspond to what the figures actually show. (c) References cited in support of a claim do not actually provide the claimed evidence.

I do not doubt that algae absorb sunlight, but I do doubt the quantitative attribution of albedo change on Greenland to algal abundance. A lot of work went into this project, and I would like to see it come to more robust conclusions. It has the potential of becoming an important paper.

*- Thank you for another round of review comments. In this document I will address each comment point by point. We have re-examined our paper in detail and overall we agree about the DISORT inversion issues. Thanks to the comments we ran a series of tests and found some unexpected behaviour in the model and have been unable to produce model outputs that we have sufficient confidence in to justify the model’s inclusion in this resubmission. For this reason, we have removed the DISORT inversion from the study. Instead, we have generated optical properties for three bulk mixtures of dusts that approximate the mineralogy and size distribution measured in the field and incorporated them into our model. In addition we have included a sensitivity study as supplementary information (Supp Info 8) that includes previously-published mineral dusts that have different mineralogies and size distributions. More details and responses to individual comments are provided below.*

**Major comments**

(1) The major comment of my first review was to point out that the imaginary part of the dust refractive index should decrease across the visible spectrum from 300 to 700 nm, not increase as shown in the first submission. In their Response to Reviewers, the authors now thank me for “pointing out the unrealistic refractive index”, but then in their revised manuscript their dust imaginary index still increases across the visible (by a factor of 2.7 from 300 to 700 nm), as shown in the new Figure 3C. [An example of Disconnect Type “a”.]

*- We appreciate the reviewer’s concerns regarding the DISORT inversions. We have reviewed the modelling in detail and we agree that the retrieval was not correct, and we have not been able to generate an imaginary refractive index that we have complete confidence in reporting in the revised manuscript. The mineral dusts did not look blue to the eye - they were very fine, near-white, dominated by quartz and feldspar minerals with very low abundance of red minerals. This is confirmed by mineralogical analysis undertaken by McCutcheon et al. (in preparation) and is consistent with previous literature (e.g. Wientjes et al. 2011). For these reasons, we have decided to remove the DISORT inversion from our paper and instead we have generated “synthetic” bulk refractive indices from our measured particle size distribution, measured relative mineral abundances and imaginary refractive indices for those minerals gathered from past literature. We have also persisted with our sensitivity study that includes typical Saharan dusts from SNICAR and low, medium and high-hematite dusts from Polashenski et al (2015), although we have moved this into Supplementary Information 8 to keep the main message in the manuscript clear. We consider this to be the most robust support for our conclusions regarding the albedo-lowering effects of mineral dusts and algae that we can feasibly produce with the available data. As you will see in the revised manuscript, this new methodology supports our original conclusion that mineral dusts have a very small direct albedo-reducing effect on the south-western Greenland Ice Sheet.*

*The relevant reworked sections of the manuscript are sections 2.5, 2.6 and 3.2, Table 1, Table 2, Fig 3B,C and Supp Info 8.*

(2) I don't want this extraordinary claim of blue dust to enter the literature on the composition of Greenland ice without further evidence. What mineral composition gives it the blue color indicated by Figure 3C? In their response to my review, the authors indicate that the mineralogy of the dust is consistent with Figure 3C, and that a paper on this topic is soon to be submitted by one of the authors (McCutcheon). A brief summary of the mineralogy in that forthcoming paper should be included in this paper; it could be cited as "unpublished data" or "manuscript in preparation".

- *We fully appreciate and agree. As explained above, we have eliminated the DISORT inversion that was generating this unusual refractive index. New data from McCutcheon et al. (in preparation) is now used to generate a "synthetic" bulk refractive index for our local mineral dusts and that paper is cited as "in preparation" as suggested. The mineralogy of these simulated local dusts is presented in the new Table 1. This is detailed in sections 2.5, 2.6 and 3.2.*

(3) The authors have ignored the request in my Major Comment #1, in which I asked the authors to show the computed albedo effect of the measured dust concentration; they continue to show just the computed albedo effect of arbitrary amounts of dust (100, 300, 500 ppm), and similarly for arbitrary concentrations of algae. At least a table is needed, giving measured dust and algal concentrations (ppm by mass). The numbers of cells are shown in Figure 2C, but these need to be combined with algal-cell size distributions to get the mass.

- *We have now incorporated new dust concentration data from McCutcheon et al (in preparation) into our study to address this comment – specifically the mean ( $342 \mu\text{g}_{\text{dust}}/\text{g}_{\text{ice}}$ ) and maximum ( $519 \mu\text{g}_{\text{dust}}/\text{g}_{\text{ice}}$ ) measured dust concentrations from  $H_{\text{bio}}$  sites. We also estimated the algal cell mass-mixing ratio from our microscope images. The mean cell abundance was  $2.9 \times 10^4$  cells/mL and the maximum was  $4.91 \times 10^4$  cells/mL. We assumed a cell density of  $0.87 \text{ g cm}^{-3}$  (Hu, 2014) and an ice density of  $0.917 \text{ g cm}^{-3}$  to calculate the mean and maximum mass mixing ratios of 349 and  $646 \mu\text{g}_{\text{algal}}/\text{g}_{\text{ice}}$ .*

*We have also continued to include additional hypothetical mass mixing ratios in our sensitivity study in Supp Info 6 to demonstrate that our conclusions are robust to a range of mass-mixing ratios.*

(4) Lines 272-273. Tedesco et al. (2013) is cited as indicating "a lack of red mineral phases". In fact, Tedesco's Figure 6a shows that both dust and algae are "red", and that dust is redder than algae; Tedesco speculated that the goethite they found in their samples had dehydrated to hematite in the drying and heating process. Goethite is the hydrated form of hematite; it is not as absorptive as hematite but its absorption coefficient likewise decreases across the visible. It is true that goethite has a yellow appearance rather than red, but it is misleading to cite Tedesco as finding "a lack of red mineral phases", since the present authors are using the adjective "red" here to characterize the spectral slope of reflectance, which increases toward the red for both goethite and hematite. [Disconnect type "c"]

- *We respectfully disagree with the reviewer on this point, for the following reasons:*

1) *Tedesco et al. (2013) identified an average of only 0.3 % goethite in the Greenland cryoconite samples, which, even if present as hematite prior to transformation during sample processing, would likely not be sufficient to account for the "red" colour in question.*

2) *Figure 6a in Tedesco et al. (2013) does not show that Greenland surface dust is redder than algae. The samples studied in Tedesco et al. (2013) were from cryoconite rather than surface ice, and therefore are unlikely to have contained glacier algae in abundances comparable to those we have measured in dark surface ice. In fact, the organic matter contained in the cryoconite is largely bacterial, cyanobacterial, humic substances, extracellular polymers and necromass – optically very different from surface algae.*

3) *Furthermore, the "red" colour measured in the mineral dust by Tedesco et al. (2013) is not representative of the natural material due to the manner in which the samples were processed. The samples were heated to 500 and 1000 degrees C, which is entering hornfelsic grade metamorphic conditions. This will have altered Fe-containing hornblende and pyroxene mineral phases thereby generating the reported "red" colour, which cannot be used to draw conclusions about the true reflectivity of the mineral dust in situ. In contrast, we*

*used a suitable chemical treatment rather than heat to remove organic matter from the samples and have data likely to represent more realistic in situ mineral optical properties.*

*We have added text to the revised manuscript to make these points clear (line 556 - 564).*

(5) Lines 518-521. “The imaginary refractive index of the mineral dust sample (Fig 3C) . . . indicating . . . scarcity of red minerals in the bare ice.” This comment is not forthright; there is no mention of the factor-of-2.7 increase of imaginary index from 300 to 700 nm, which indicates not merely a scarcity of red minerals but actually a dominance of blue minerals. Don’t be so timid! You must highlight this strange imaginary index, and point out how it contradicts the behavior reported by Tedesco et al. 2013. [Disconnect Type “b”]

*We have reworked this section after removing the inverse modelling from our study.*

(6) Lines 539-541, discussing Figure 3B. Albedo spectra for algae “downsloping with increasing wavelength between 0.35 and 0.45 microns . . . and a gentle increase to 0.70 microns. These spectral features are consistent with our field spectra for algal ice” This is not true. The field spectrum for algal ice (Figure 2B) starts at 0.40 not 0.35, and shows albedo increasing, not downsloping, from 0.40 to 0.45 microns. And Figure 2B (field) shows a steep increase from 0.6 to 0.7 microns, whereas the dashed line in Figure 3B (model) is flat from 0.6 to 0.7. [Disconnect Type “b”]

*We have reworked this section and made more accurate descriptions of the spectral albedo.*

(7) Lines 574-575. “. . . algal cells had a greater albedo-reducing effect than mineral dusts in north-west Greenland (Aoki et al. 2013).” This summary of the Aoki paper is misleading. Aoki et al. did conclude that the imaginary index of algae was larger than that of mineral dust, but did not conclude that most of the albedo reduction was due to algae. Their total impurity mass in the ice was 1127 ppm, of which 29 ppm (2.6%) was organic carbon (algae), so ~1100 ppm was dust. Their Figure 4b shows that they could explain most of the albedo reduction by 1000 ppm dust; the remainder (which looks like about 5% to me) is then attributed to algae. [Disconnect Type “c”]

*We revisited Aoki et al. (2013) and have removed the citation from our manuscript for the following reasons. There is conflation between surface impurities, cryoconite and surface dust. Their figure 2B shows what those authors consider to be a “cryoconite” surface, which is what we would now consider to be a mixture of surface dust and glacier-algal biomass similar to that included in our study. Cryoconite is properly defined as: discrete granules of biological and mineral material that typically have a very dark brown-black colour and reside on the floor of cryoconite holes unless the local energy balance conditions favour them being evacuated onto the bare ice surface. For this evacuation to happen, turbulent heat fluxes must exceed radiant heat fluxes for a period of several days (i.e. persistent cloudy conditions) so that the weathered surface ablates downwards to expose smooth solid ice and the cryoconite holes that occupy the weathered crust “melt out”. The morphology of the ice shown in their Figure 2B is not consistent with this process having occurred, and this is further confirmed by the sentence “there were also cryoconite holes (water-filled cylindrical melt-holes with cryoconite on the bottom)”. If there are cryoconite holes present, any dispersed cryoconite must be spatially discrete, and the distributed impurities they refer to as cryoconite must actually be a dust and algae mixture comparable to that observed at our field site. Furthermore, they have not generated optical properties for the actual dust found at their field site, but simply imported dust optical properties from a pre-existing library where the mineralogy is assumed to be mostly illite, calcite, feldspar and chlorite derived from Asian dust samples (see Aoki et al, 2005) that are very different to our local mineralogy (and perhaps to the true mineralogy at their field site too). For these reasons, it is not helpful to compare Aoki et al.’s (2013) interpretation of their albedo data – certainly not their separation of mineral and biological effects - to ours.*

*Another important point is that where Aoki et al. (2013) refer to algae, they are making reference to the bright red snow algae that grows on melting snowpacks. This is taxonomically, morphologically and optically very different to our glacier algae.*

Aoki et al. (2005): Sensitivity Experiments of Direct Radiative Forcing Caused by Mineral Dust Simulated with a Chemical Transport Model *Journal of the Meteorological Society of Japan*, Vol. 83A, pp. 315--331, 2005315

(8) Lines 544-546, and Figure 2C. The authors point out that mineral dust particles can “act as substrates for the formation of low-albedo microbial-mineral aggregates”. This suggests an alternative explanation of the correlation shown in Figure 2C: The algae may be concentrated in patches of ice that have high mineral content, so the cell count then would be correlated with the albedo reduction caused by dust.

*We agree, this is a central question that we have attempted to address using our radiative transfer modelling.*

(9) Section 3.3, lines 577-610. This section analyzes the albedo trough centered at 1.02 microns, following Nolin and Dozier (2000). Nolin and Dozier found the 1.02-micron trough to be deeper for lower albedo (coarse-grained snow), whereas Supp Info 5B here shows the opposite, namely deeper trough for higher albedo. The 1.02-micron feature is therefore not useful for discussing “indirect effects of algae”. The entire section 3.3 should therefore be shortened to just the last four lines 607-610, making a single sentence starting “Algal growth is stimulated . . . “ [Disconnect Type “c”]

*Yes, the relationship does show a deeper trough for higher albedo. We consider this to be an artefact of an overall lower albedo across the entire spectrum effectively “dampening” all of the reflectance features. However, the point we were making was simply that there is albedo reduction in the NIR associated with increased LAP loading as well as in the visible wavelengths, indicative of secondary or “indirect” albedo reducing processes related to grain size and shape, melt water accumulation, etc. We have dramatically shortened this section as suggested, but kept two additional introductory sentences to make the point of the paragraph clear to a wide readership, and hope that this is acceptable.*

2(10). Figure 4ABC. Half of the solar energy is at wavelengths <0.7 microns, and 80-90% (depending on cloud thickness) is at wavelengths <1.0 microns. In these figures, the peculiar wiggles in the visible region, the most energetically important part of the spectrum, are squeezed into a tiny region on the far left of the figures. These wiggles need to be discussed and explained in the text, and the figure should be redrawn, for a domain 0.3-1.5 microns instead of 0-5 microns.

*These figures related to our DISORT inversion and have therefore been discarded.*

### **Minor comments.**

line 206. “. . . they are large, far outside the domain of Mie scattering”. Mie theory is not restricted to small size-parameters. Admittedly Mie calculations do become expensive for large size-parameters.

*We appreciate that technically Mie calculations can be solved for any size of particle, but we also acknowledge that there is a huge computational cost associated with solving them for particles in the size range of our glacier algae. The Mie scattering domain is commonly described in the literature as  $2 > \text{size parameter} < 2000$ . We acknowledge the point and have changed the text accordingly, to:*

*“they are large, making Mie calculations impractically computationally expensive” (line 202 in revised manuscript)*

line 247. “real refractive index”. I think you mean imaginary refractive index, or complex refractive index.

*This has been corrected.*

line 262. “four global average dusts from Flanner et al. (2007)”. The Flanner 2007 paper concerns black carbon; it contains no information about dust. Give the correct reference. [Disconnect Type “c”]

*The citation as been updated to Flanner et al. (2009) where the dust aerosols in SNICAR were discussed for the first time (citation now moved to Supp Info 8): Flanner, M.G., Zender, C.S., Hessm P.G., Mahowald,*

*N.M., Painter, T.H., Ramanathan, V., Rasch, P.J., Springtime warming and reduced snow cover from carbonaceous particles. Atmospheric Chemistry and Physics, 9: 2481-2497, 2009.*

line 320. “CI” has not yet been defined.

*This has been corrected.*

Line 478. Change 2B to 2D.

*This has been corrected*

Line 484. Change 2C to 2B.

*This has been corrected*

Line 488. Change 2C to 2D.

*This has been corrected – we think the reviewer meant 2D → 2C.*

Figure 2B. The labels Hbio, Lbio, CI, SN should be defined in the figure caption.

*This has been updated*

Figure 6. This is a nice figure showing the contrast between 2016 and 2017.

*Thank you*

Table 2 should be rearranged. Seeing the numbers from different methods side-by-side would help the reader compare them. For example, the first line (water albedo) would read “0.31, 0.08, 0.08”.

*This has been updated as requested (now presented as Table 3 in revised manuscript)*

### **Spelling and punctuation.**

line 181. Change gluteraldehyde to glutaraldehyde.

*This has been corrected*

line 290. “the the”

*This has been corrected*

line 983. distributed

*This has been corrected*

line 1240-1245 (Table 1). “ug” is not the correct symbol for micrograms. Use the Greek lower-case mu.

*This has been corrected*

### **Additional Comments**

*We also acknowledge receipt of four comments raised separately by email directly to the lead author. Since these were all related to a figure that is no longer included in the revised manuscript (being associated with the DISORT mdoel inversion) we consider them addressed.*

## Response to Reviewer 2 comments on Glacier algae accelerate melting on the south-western Greenland Ice Sheet by Cook et al.: Round 2

In this revision, Cook et al. provided more details on methods as suggested by reviewers. The fieldwork and radiative transfer modeling components are very important and valuable for the cryosphere community to understand better the impurity properties. However, some key/core information/figures are still lacking for the section using UAV and Sentinel-2 remote sensing data assisted by ASD field spectra to conduct image classification. In addition, there are some contradictory and inconsistent arguments throughout the text. These problems need to be resolved:

*We thank the reviewer for the second set of comments. We have provided a point-by-point response below:*

**1) I asked the authors to provide the ASD spectra (resampled to UAV bands and Sentinel-2 bands) compared against the real UAV and Sentinel-2 spectra, but I didn't see them in this revision. I think the authors should at least provide a figure showing how consistent the ASD resampled spectra are with the UAV and Sentinel-2 spectra. This is very important for the image classification, because UAV spectra and Sentinel-2 spectra have uncertainties of atmospheric correction and other radiation correction procedures. If they don't match very well, using ASD-resampled spectra to train the RF or other classifiers is not convincing. Although the authors claim that the RF method is advanced and novel for studying the cryosphere, it is essentially an image classification problem and subject to basic image classification rules. The authors classified surface types into snow, clean ice, cryoconite, water, low biomass algae, and high biomass algae. Please provide a figure showing the comparison between the ASD reduced spectra and the UAV and Sentinel-2 spectra for each class, and label the bandwidth for each UAV and Sentinel-2 band. If the spectral curves of these classes are highly correlated, the whole classification problem will become a thresholding problem, and the derived 'high biomass algae' will be equivalent to 'dark ice'. Without providing this information (i.e. actual plots), the classification method is not solid, and the classification results are not convincing.**

*We provide below a series of five plots showing ASD reflectance plotted against UAV reflectance for each of the five UAV bands (Figure 1: UAV on the y-axis and ASD on the x-axis). These measurements were made for the points in our UAV imagery where measurements were also made using the ASD field spectrometer. The blue markers show the ASD spectra plotted against uncorrected UAV spectra. The red markers show the same data after a systematic offset was corrected in order to calibrate the UAV against the ASD field spectra (the magnitude of the offset is given in the header of each plot).*

*From these plots it is clear that following subtraction of the systematic offset from each UAV band there is a close match between the resampled ASD and UAV reflectance that supports the validity of our classifier. We cannot co-locate centimeter scale ASD measurements on the 20 m resolution Sentinel-2 imagery so the*

equivalent plots cannot be generated for ASD vs Sentinel-2. We also direct the reviewer to Figure 5C in Tedstone et al. (in review: <https://www.the-cryosphere-discuss.net/tc-2019-131/tc-2019-131.pdf>, copied below as Figure 2) where the albedo measured by Sentinel-2 and our offset-corrected UAV are compared for several flights made during the same field season at the same field site, with the black crosses representing the S2 albedo and yellow crosses representing UAV albedo.

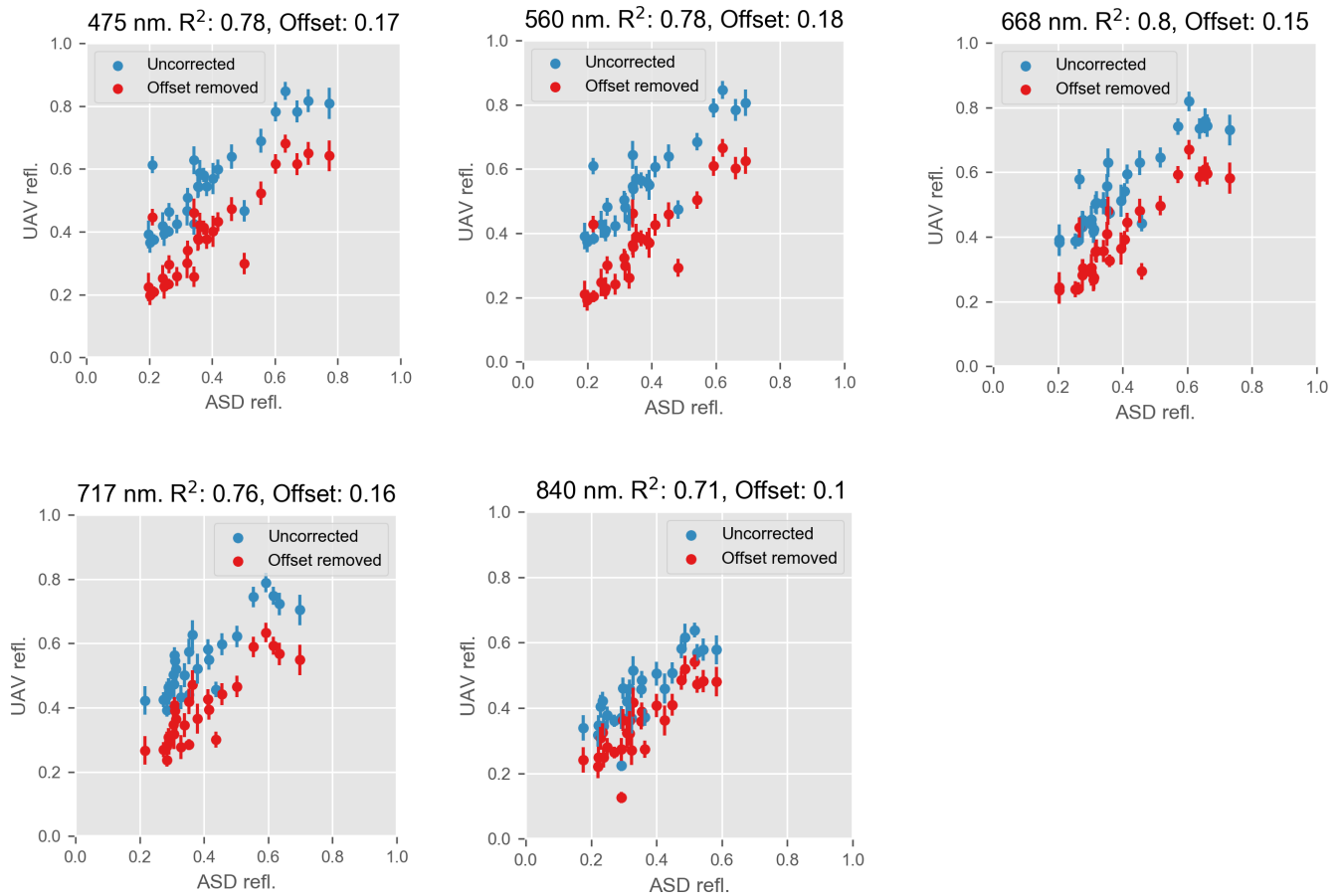


Figure 1: UAV reflectance plotted against ASD reflectance for each UAV band, in uncorrected (blue) and corrected (red) form.

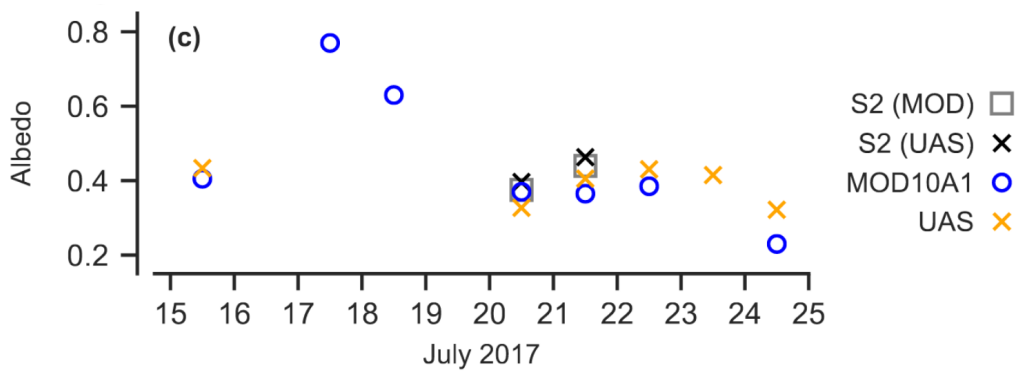


Figure 2: UAV and S2 albedo for days with coincident UAV flights and S2 overpasses during our 2017 field season from Tedstone et al. (in review).

As requested, we also provide a comparison of the reflectance values for each surface class in each waveband (Figure 3 and Figure 4). In Figure 3 close correspondence between the reflectance values measured by the UAV and the ASD field spectrometer is demonstrated, and there is clear separation between the classes, supporting the validity of the classifier. Figure 4 shows that there is a weaker correspondence between the reflectance measured by the ASD and Sentinel-2, but there is generally still separation of the classes. However, there is poor separation in the HA class at the short visible wavelengths. We highlight two key features of our approach:

1. The ambiguity in the short visible wavelengths demonstrates why information from all nine bands is required and therefore why our classifier is preferable to a threshold. Our classifier uses information from all 9 bands to separate the classes, which provides a degree of resilience to ambiguity in the short visible wavelengths, whereas a simple thresholding approach would be more likely to confuse the classes.

2. Regarding the Sentinel-2 classifier specifically, whilst in principle there is potential for misclassification of LA as HA, this is unlikely in practise because HA patches, as shown by our UAV observations, are not spatially expansive over metres+ scales and therefore all HA surfaces detected by Sentinel-2 are mixed with other, brighter surface types. The Sentinel-2 classifier therefore remains conservative. In the cases where HA is identified in Sentinel-2 imagery, we would still expect mean reflectance of these pixels to be higher than in the UAV and ASD spectra because the area-averaged reflectance is pushed up by mixing of HA with brighter surrounding surfaces, and indeed we can see this is the case in Figure 4 – the darkest end-members found at the 30 cm ASD scale are simply not found at the 20 m Sentinel-2 scale.

We have discussed this scale issue in the manuscript, and now add Figures 1, 3 and 4 to Supp Info 6. We also direct the reviewer to Tedstone et al (in review: <https://www.the-cryosphere-discuss.net/tc-2019-131/>) where these issues are discussed in more detail, including further evidence for coarser spatial scales leading to higher algal detection limits (i.e. a conservative algal classifier).

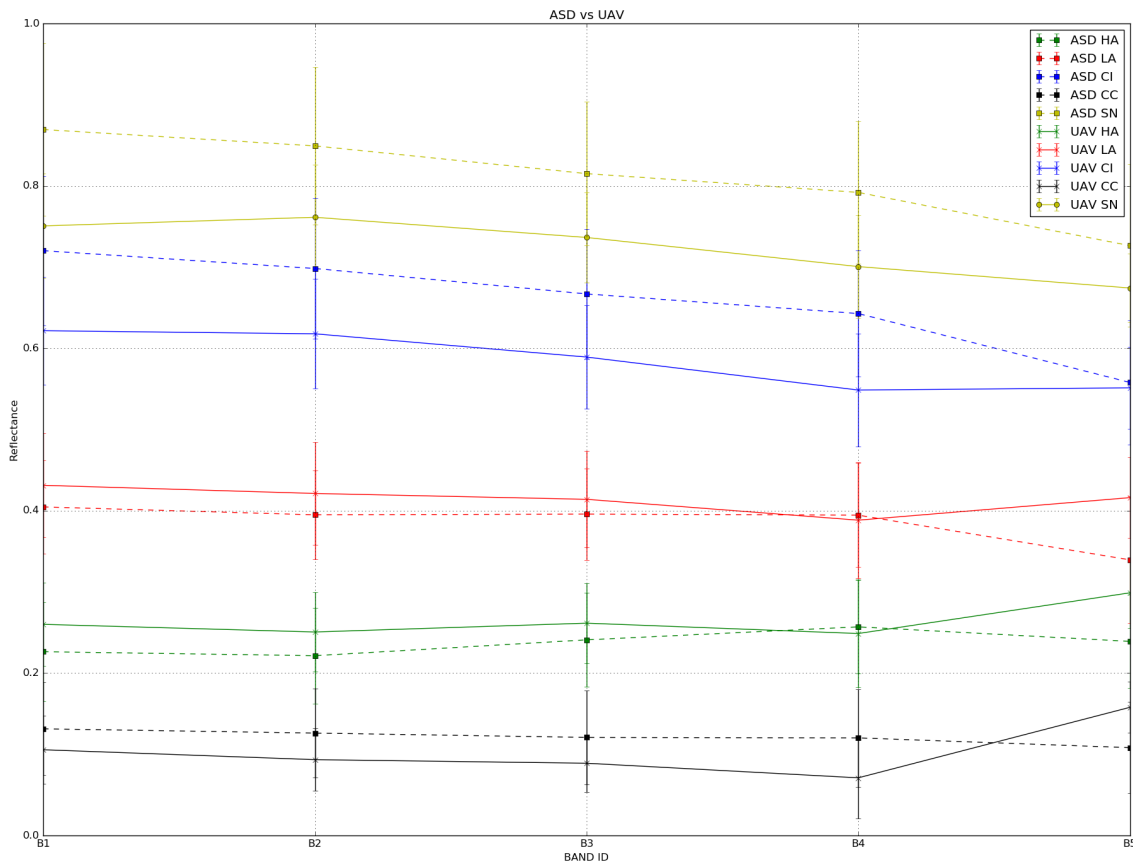


Figure 3: Comparison of mean reflectance values for each surface class from the ASD and UAV data.

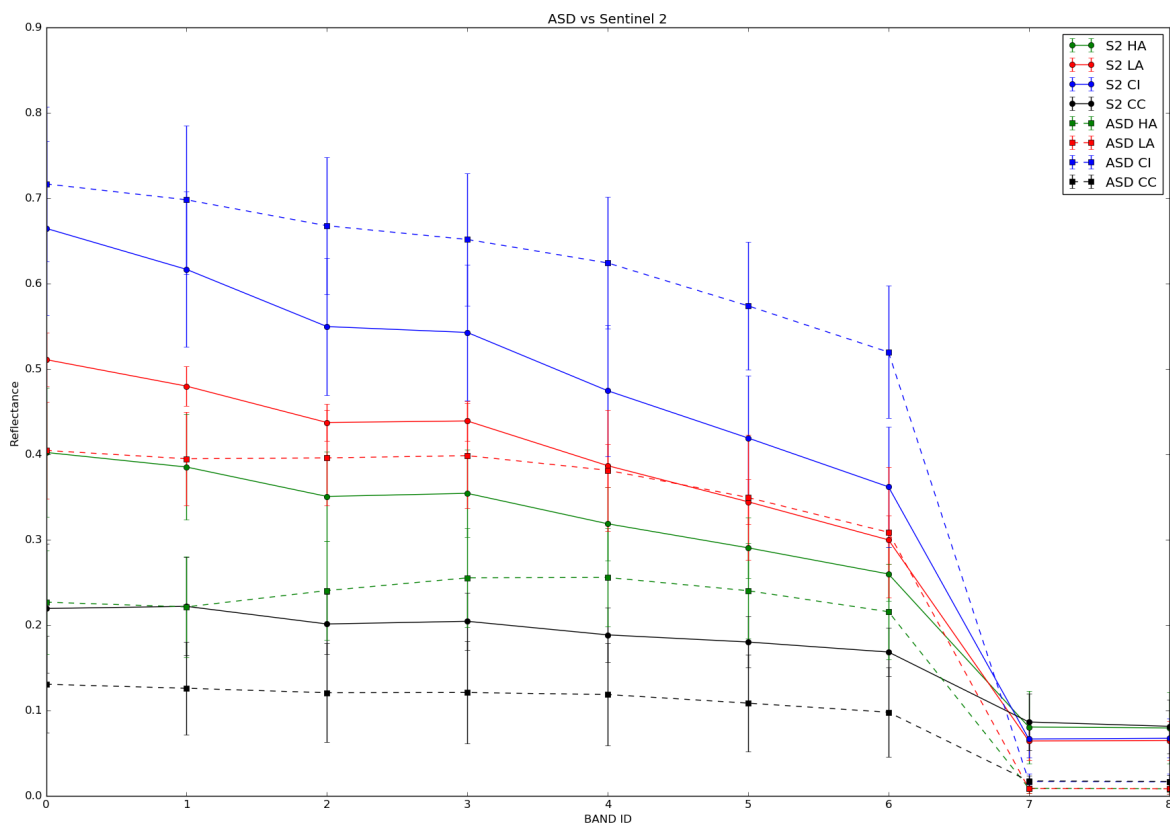


Figure 4: Comparison of mean reflectance values for each surface class from the ASD and Sentinel-2 data.

2) The arguments regarding glacier algae and red mineral dust are contradictory. In the introduction section, when the authors mentioned the recent study by Wang et al. (2018) who proposed to use the reflectance ratio between 709 nm and 673 nm to map ice algae in southwest Greenland, it is claimed that ‘the red-edge is potentially vulnerable to false positives due to red mineral dusts (Seager et al. 2005; Cook et al. 2017b)’. On page 8 line 260-265, the authors mentioned again that red dust has ‘similarly shaped spectral albedo to glacier algae’. However, throughout the paper and the two referenced papers, I didn’t find any convincing evidence (i.e. data) showing that the red dust can indeed mask out the chlorophyll signature at red-NIR spectrum. If the red dust is indeed very similar to glacier algae in spectral properties, then no practical methods would exist to separate them regardless of the spatial resolution of the remote sensing data, which means the RF method cannot work as well. The authors claim later in the manuscript (on page 14 line 500-510) that the chlorophyll-a signal between 670 and 710 nm (red edge) is uniquely biological and use this red-edge (Painter et al., 2001 and Wang et al., 2018) to support their results. On page 16 line 550-555, the authors again argue that red minerals occur only in very low concentrations and would have a negligible effect on the ice optics. These arguments are contradictory, with the later arguments supporting the red-edge method used for mapping algae in southwest Greenland. I suggest the authors should properly acknowledge previous studies.

*There is precedent in the literature for the red-edge method being confused by red dusts. A famous example is that the red-edge was cited in the 1950s - 1960s as evidence for chlorophyll-containing green plants on the surface of Mars, but of course this was later revealed to be red dusts (see Seager et al. 2005; Sagan and Pollack, 1969: <https://www.nature.com/articles/223791a0>). Sparks et al. (2009) shows similarity in spectral edges between vegetation and iron oxide (<https://www.pnas.org/content/pnas/early/2009/04/28/0810215106.full.pdf>) that they state could lead to false positive bio-detection in a red-edge study.*

*The popularity of the red-edge method arises from its widespread use in vegetation mapping where low spatial and spectral resolution sensors can be applied with confidence because there is an abundance of a priori knowledge about the surface reflectance and end-member spectral libraries. This is not true in our case. It is only with our field samples and our radiative transfer model that we can now discount the effects of red dusts upon ice surface darkening in this region of the GrIS. Previous to our study, there has been scarce evidence to support the application of the red-edge method for detecting glacier algae. While the red-edge method does a fair job at classifying the ice surface in our case, it is outperformed by our RF classifier. The feature importances are highest at blue and green wavelengths for our classifier, suggesting that the red-edge classifier overlooks important spectral information for classifying the ice surface. We therefore see no reason to employ a lesser method when we have a better-performing one available to us.*

Where we describe the algal and red-mineral spectra as similar we mean that both of these light-absorbing particles preferentially absorb light in the short visible wavelengths. Sensors with low spectral resolution that cannot resolve uniquely biological features such as the 680nm absorption feature or the “chlorophyll bump” at 550 nm, or the “flattened” spectrum across the blue-green wavelengths in the case of glacier-algae will struggle to separate them. However, at our field site we have shown that in this study the low abundance of red mineral phases means the red-edge method is applicable as a rudimentary life-detector. However, our RF classifier is more accurate as it uses information from additional wavelengths as well as the red-NIR. The red-edge is simply a presence/absence detector and is unable to separate the ice surface into multiple classes as our RF classifier does. The red-edge also relies on sufficient spectral resolution in the red-NIR part of the spectrum that is not available on many sensors, whereas our method of resampling hyperspectral data can be applied to any sensor by retraining on new subsets of the spectra. Furthermore again, with highly variable ice albedo that in itself can range from  $<0.3$  to  $>0.7$ , the red-edge can be dampened or deepened independently of changes to the algal abundance – classifiers sensitive to shorter wavelengths are more robust to this as the majority of the light absorption by algae occurs at shorter visible wavelengths. Therefore, there are several compelling reasons to use our classifier over a simple red-edge classifier. We also note that the 680 nm feature is not a “red-edge”. Rather, it is a discrete absorption feature centred on 680 nm whose presence is diagnostic for chlorophyll-a and whose area scales with chlorophyll-a concentration (Painter et al. 2001). It can only be reliably applied to hyperspectral data as the method relies upon interpolation between the shoulders of the feature and the calculation of the area beneath this interpolated line. We note that we did not describe the red-edge as “uniquely biological” - we only described the 680 nm absorption feature as uniquely biological. For the red-edge we simply state that it is widely used to detect green vegetation in other environments.

In response to the reviewer comments we have adjusted our description of the previous research in the revised manuscript (lines 100-110) so that it now reads:

“Recently, Wang et al. (2018) applied the vegetation red-edge (difference in reflectance between 673 and 709 nm) to map glacier algae over the south-western GrIS using Sentinel-3 OLCI data at 300 m ground resolution.”

**3) In the response, the authors said ‘We attempted to use the vegetation red-edge on our spectra and achieved only ~80% accuracy for identifying algal ice compared to our random forest classifier that achieves >95% accuracy.’ How many samples were used to calculate the accuracy? Were the training samples also used to obtain the 95% accuracy? If they were, it is not a fair comparison. Actually, for remote sensing classification problems, 80% accuracy is quite high. Why not use this information to cross-validate your method? It seems to me that the red-edge method actually supports your classification results.**

We agree with the reviewer that the red-edge method does offer broad support for our classification method when applied to the full-resolution ASD spectra. It was applied to all of our algal spectra.

The RF classifier was also applied to all of our algal spectra, divided into the training set and test set. The ratio of training to test samples was 80:20, not 70:30 as was accidentally reported in the previous version of the manuscript, giving 45 samples in the test set. The performance of the classifier on the training and test sets were similar, suggesting the trained model generalises well to unseen instances. The accuracy, precision, recall and F1 scores for the RF classifier and several other classifiers that were trained for comparison are already available in Supp Info 5 for both the UAV and Sentinel-2 classifiers.

**4) Page 7 line 227-228, please show simulation results in supplementary information.**

We have added six simulations using different cell sizes to our supplementary information (Supp Info 2). The spectral and broadband albedo resulting from 10 – 1000  $\mu\text{g/g}$  in the upper layer are presented as in Figure 5 below:

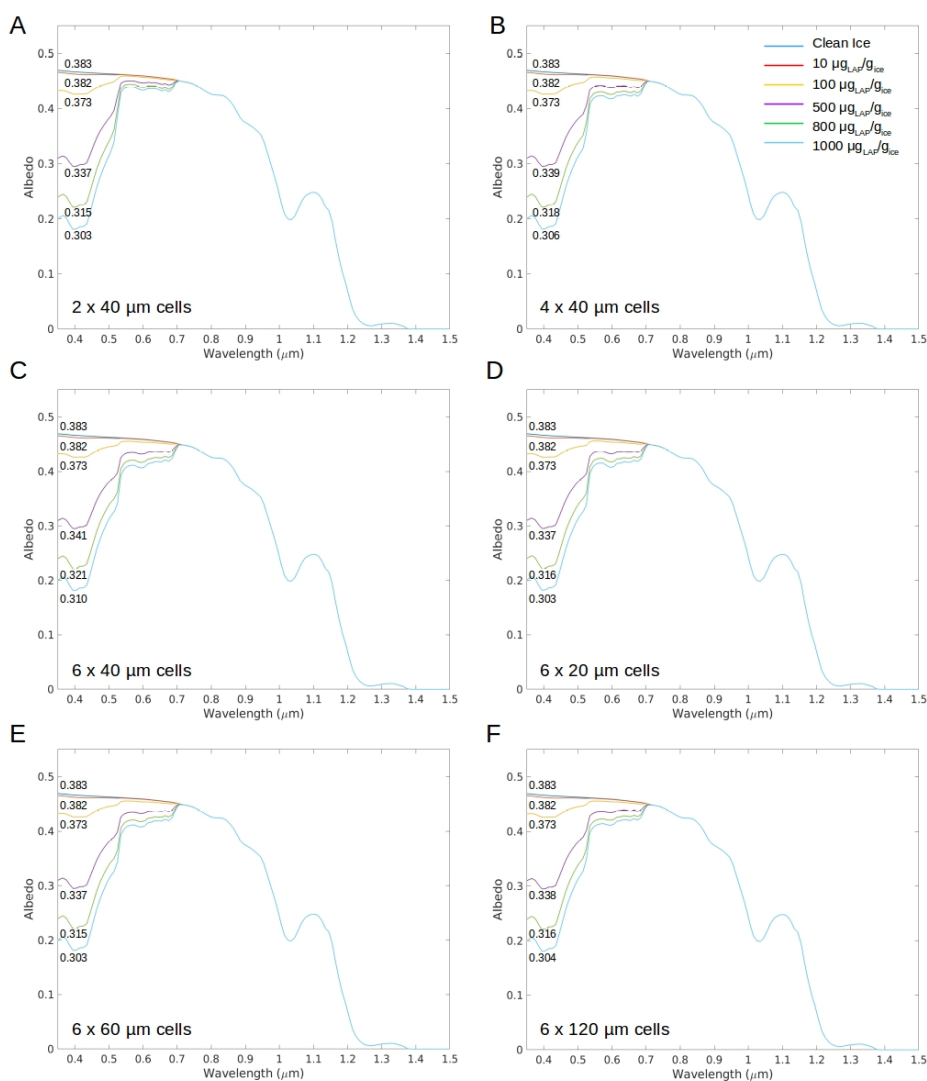


Figure 5: Spectral albedo for ice surfaces loaded with algae in mass-mixing ratios between 10 – 1000  $\mu\text{g/g}$ . Broadband albedo are printed below each curve.

**5) Page 7 line 376, does this mean that there are  $231 \times 0.7 = 162$  training samples and  $231 \times 0.3 = 69$  test samples? Were all accuracy tests based on 69 samples? In this case, how many samples for each class were available to test the classifiers?**

*The training-test split was actually 80:20 in the revised manuscript, we apologise for missing this update to the text. The sample instances in the test-set were as follows: Cryoconite: 6, Clean Ice: 5, Heavy Algae: 16, Light Algae: 7, Snow: 5, Water: 6. This gives a total of 45 instances (20% of 231).*

**6) Page 11 line 387-390, I don't quite understand the logic here, are the authors trying to say that they want to build an endmember library using ASD spectra? How can it be certain that using 'pure' spectra can get better accuracy for classifying images (with spatial heterogeneity within each pixel) rather than directly labeling the images (to obtain training sets)?**

*The reviewer is correct that we have built an end-member spectral library using ASD spectra. We consider this to be the only justifiable way to classify the ice surface. We deliberately avoided direct image-labelling because the labels in the training set would simply be guesses at the surface composition. Labelling images in this way may produce more data, but of lower quality since there will necessarily be label ambiguity. We measured the spectral reflectance of homogenous areas and analysed the ice composition in the laboratory, so we are sure of our labels. The field-of-view of the spectrometer was small so we can be confident that the spectra are representative of a single surface class rather than an area containing multiple surface types. The price of this is reduced data abundance as the reflectance data acquisition and sample processing is expensive and time-consuming, but the benefit is high data quality. With the current scarcity of knowledge/data on light absorbing particles and the highly variable physical structure of the ice in this area, directly-labelling images would suffer from high label uncertainty. We discuss these issues in lines 393 – 399.*

**7) Supp info 6: this figure is not easy to read, please directly give the correlation numbers in a table format, along with the number of test samples.**

*Unfortunately the specific instances used to train and test the Sentinel-2 classifier were not saved when we saved the model, the summary metrics and the figure, so we are unable to provide those values. However, we have provided the overall performance metrics (accuracy, precision, recall, F1: Supp Info 5) and the confusion matrix plots that clearly demonstrate that the classifier performs well and generalises well to new instances. An 80:20 ratio of training:test samples was used, meaning 45 instances were available in the test set, and multiple instances were available in the test set for every class.*

**8) I'm confused by your study area. On page 12 line 420, "The area of interest was the "common area" defined by Tedstone et al. (2017) bounded within the latitudinal range 65 – 70 N, and is equal to that used by Wang et al. (2018)". Figure 1 and Figure 5 show an area between 67.615N and 67.599N, which is much smaller than 65 – 70 N. Which one is the study area? It seems that the UAV and Sentinel-2 only cover a very small portion.**

*The UAV image area was a 200 x 200 m area which was located inside a larger Sentinel-2 tile (65.615 – 67.599 N). We upscaled to 65-70N in our runoff modelling. We have clarified further in our methodology (lines 133-135 in the revised manuscript).*

**9) Section 2.10 and 3.7. Thanks to the authors for providing more details here. However, this part is still not very clear to me. When the authors generalized the runoff estimate (simulated based on three weather stations) over the entire region (65 – 70 N?), are the area percentages of low biomass algae and high biomass algae based on classification results over the 200\*200 m UAV region and the 67.615-67.599N Sentinel-2 region to generalize to the entire region based on the bare ice area and dark ice area derived from MODIS data (500 m resolution)? If so, did the authors consider issues associated with different spatial scales? The authors pointed out that "The higher detection limit for algae with decreasing ground resolution makes our estimate of spatial coverage from Sentinel-2 conservative. We highlight that this will have a much larger effect on studies aiming to quantify cell abundance using Sentinel-3 where the ground resolution is 300 m." (page 19 line 669). Table 3 shows the area percentage of different classes, total algae is 78.5% on UAV, 57.99% on Sentinel-2 (2016) and 58.87% on Sentinel-2 (2017). Is this the evidence that supports the argument that Sentinel-2 estimate is conservative? If so, this doesn't make sense since totally different areas are being compared (200\*200m vs 10000\*10000m). Please clarify. Given the spatial scale issues, it is incorrect to directly extrapolate the area percentage from centimeter resolution and 20m resolution to MODIS 500 m resolution. Please justify the methods.**

*We have provided a runoff range forced by our upper and lower estimate of algal surface coverage. The upper estimate is from our classified UAV image. We specifically caveat in the manuscript that this is an upper estimate because we cannot be sure that the coverage is representative across the upscaling area. The lower bound is from our classified Sentinel-2 image. Again, we specifically caveat that this is a lower bound because the coarser spatial scale introduces surface heterogeneity as discussed in the response to earlier questions, which makes detection of algae-laden surfaces at coarser scales increasingly conservative. This is true both at the scale of individual pixels (since patch sizes are generally much smaller than 20m) and at the scale of the entire image (since ice from outside the dark zone is included in the 100 x 100 km tile). These likely explain the differences in coverage presented in our Table 3. This is explained in section 3.7 as follows:*

*Line 680: “At the same time, our Sentinel-2 remote-sensing underestimates algal coverage because  $H_{bio}$  patches are often too small to be resolved at 20 m pixel resolution (Tedstone et al. in review). Therefore, we used the spatial coverage determined by our Sentinel-2 classification as a lower bound, and spatial coverage determined by our UAV classification as an upper bound on our estimate of total runoff attributed to the presence of algae.”*

*The reviewer is correct that we have upscaled to the 65-70N (“south-western”) region. We agreed with the reviewer in the initial round of review comments that upscaling to the entire western coast of the GrIS was excessive given the field measurements were all from the Kangerlussuaq region; however, upscaling over the south-western GrIS is justifiable, especially since there is literature precedent for upscaling over this region. We have delineated the extent of the dark zone using MODIS using protocols from the past-literature (Tedstone et al. 2017; Shimada et al. 2016) and applied our upper and lower algal coverage estimates to force the runoff model, over an area where we expect our field measurements and observations to be representative. We have therefore applied our classifier to UAV and Sentinel-2 images to determine realistic coverage estimates and applied them over the dark zone as defined using MODIS thresholds consistent with previous studies. We also point to the paper currently in open review in The Cryosphere by Tedstone et al. (<https://www.the-cryosphere-discuss.net/tc-2019-131/>), where inter-sensor comparisons and cross-scale comparisons between our field, UAV and satellite remote sensing data are quantified and examined in detail.*

*We have therefore considered the issues raised in the comment above and mitigated them by providing a range of estimates.*

# Glacier algae accelerate melt rates on the south-western Greenland Ice Sheet

Joseph M. Cook<sup>1,2</sup>, Andrew J Tedstone<sup>3</sup>, Christopher Williamson<sup>4</sup>, Jenine McCutcheon<sup>5</sup>, Andrew J. Hodson<sup>6,7</sup>, Archana Dayal<sup>1,6</sup>, McKenzie Skiles<sup>8</sup>, Stefan Hofer<sup>3</sup>, Robert Bryant<sup>1</sup>, Owen McAree<sup>9</sup>, Andrew McGonigle<sup>1</sup>,  
5 Jonathan Ryan<sup>12</sup>, Alexandre M. Anesio<sup>13</sup>, Tristram D.L. Irvine-Fynn<sup>11</sup>, Alun Hubbard<sup>14</sup>, Edward Hanna<sup>15</sup>, Mark Flanner<sup>16</sup>, Sathish Mayanna<sup>17</sup>, Liane G. Benning<sup>5,17,18</sup>, Dirk van As<sup>19</sup>, Marian Yallop<sup>4</sup>, James B. McQuaid<sup>5</sup>, Thomas Gribbin<sup>3</sup>, Martyn Tranter<sup>3</sup>.

<sup>1</sup> Department of Geography, University of Sheffield

10 <sup>2</sup>Institute of Biological, Environmental & Rural Sciences, Aberystwyth University, Aberystwyth, UK

<sup>3</sup> Center for Glaciology, University of Bristol

<sup>4</sup> Department of Biosciences, University of Bristol

<sup>5</sup> School of Earth and Environment, University of Leeds

<sup>6</sup> Department of Geology, University Centre in Svalbard

15 <sup>7</sup> Department of Environmental Sciences, Western Norway University of Applied Sciences, 6856 Sogndal, Norway

<sup>8</sup> Department of Geography, University of Utah

<sup>9</sup> Faculty of Science, Liverpool John Moores University

<sup>10</sup> School of Geosciences, University of Sydney, Sydney, NSW 2006, Australia

20 <sup>11</sup> Department of Geography and Earth Science, Aberystwyth University, Wales, SY23 3DB, UK

<sup>12</sup> Institute at Brown for Environment and Society, Brown University, Providence, Rhode Island, USA

<sup>13</sup> Department of Environmental Science, Aarhus University, 4000 Roskilde, Denmark

<sup>14</sup> Centre for Gas Hydrates and Climate, University of Tromsø, Norway

<sup>15</sup> School of Geography and Lincoln Centre for Water and Planetary Health, University of Lincoln

25 <sup>16</sup> University of Michigan, Ann Arbor, Michigan, USA

<sup>17</sup> German Research Centre for Geosciences, GFZ, Potsdam, Germany

<sup>18</sup> Department of Earth Sciences, Free University of Berlin, Germany

<sup>19</sup> Geological Survey of Denmark and Greenland, Copenhagen, Denmark

*Correspondence to:* Joseph Cook ([joc102@aber.ac.uk](mailto:joc102@aber.ac.uk))

30 **Abstract.** Melting of the Greenland Ice Sheet (GrIS) is the largest single contributor to eustatic sea level and it is amplified by the growth of pigmented algae on the ice surface that increase solar radiation absorption. This biological albedo-reducing effect and its impact upon sea level rise has not previously been quantified. Here, we combine field spectroscopy with a radiative transfer model, supervised classification of UAV and

satellite remote-sensing data and runoff modelling to calculate biologically-driven ice surface ablation. We demonstrate that algal growth led to an additional 4.4 – 6.0 Gt of runoff from bare ice in the south-western sector of the GrIS in summer 2017, representing 10 – 13 % of the total. In localised patches with high-biomass accumulation, algae accelerated melting by up to  $26.15 \pm 3.77$  % (standard error). 2017 was a high albedo year, so we also extended our analysis to the particularly low-albedo 2016 melt season. The runoff from the south-western bare-ice zone attributed to algae was much higher in 2016, at 8.8 – 12.2 Gt, although the proportion of the total runoff contributed by algae was similar at 9 – 13%. Across a 10,000 km<sup>2</sup> area around our field site, algae covered similar proportions of the exposed bare ice zone in both years (57.99 % in 2016, 58.89 % in 2017), but more of the algal ice was classed as “high-biomass” in 2016 (8.35 %) than 2017 (2.54 %). This interannual comparison demonstrates a positive feedback where more widespread, higher biomass algal blooms are expected to form in high melt years where the winter snowpack retreats further, earlier, providing a larger area for bloom development and also enhancing the provision of nutrients and liquid water liberated from melting ice. Our analysis confirms the importance of this biological albedo feedback and that its omission from predictive models leads to the systematic underestimation of Greenland’s future sea level contribution, especially because both the bare-ice zones available for algal colonization and the length of the biological growth season are set to expand in the future.

## 50 **1 Introduction**

Mass loss from the Greenland Ice Sheet (GrIS) has increased over the past two decades (Shepherd et al., 2012; Hanna et al., 2013) and is the largest single contributor to cryospheric sea level rise, adding 37% or 0.69 mm yr<sup>-1</sup> between 2012-2016 (Bamber et al., 2018). This is due to enhanced surface melting (Ngheim et al., 2012) that exceeds calving losses at the ice-sheet’s marine-terminating margins (Enderlin et al., 2014; van den Broeke et al., 2016). Surface melting is controlled by net solar radiation, which in turn depends upon the albedo of the ice surface, making albedo a critical factor for modulating ice-sheet mass loss (Box et al., 2012; Ryan et al. 2018a). The largest shift in albedo occurs when the winter snow retreats to expose bare glacier ice. However, there are several linked mechanisms that then change the albedo of the exposed ice and determine its rate of melting, including meltwater accumulation, ice surface weathering and the accumulation of light-absorbing particles (LAPs), such as soot (Flanner et al., 2007) and mineral dust (Skiles et al., 2017). Photosynthetic algae also reduce the albedo of the GrIS (Uetake et al., 2010; Yallop et al., 2012; Stibal et al., 2017; Ryan et al., 2017, 2018b). Despite being identified in the late 1800’s (Nordenskiöld, 1875) their effects have not yet been quantified, mapped or incorporated into any predictive surface mass balance models (Langen et al. 2017; Noel et al., 2016; Fettweis et al. 2017). Hence, biological growth may play an important yet under-appreciated role in the melting of the Greenland Ice Sheet and its contributions to sea level rise (Benning et al., 2014).

The snow-free surface of the GrIS has a conspicuous dark stripe along its western margin which expands and contracts seasonally, covering 4 - 10% of the ablating bare-ice area (Shimada et al., 2016). The extent and darkness of this “Dark Zone” may be biologically and/or geologically controlled (Wientjes et al., 2011; 2016; Tedstone et al., 2017; Stibal et al., 2017). There is a growing literature demonstrating the albedo-reducing role played by a community of algae that grow on glacier ice on the eastern (Lutz et al. 2014) and western (Uetake et al. 2010; Yallop et al. 2012; Stibal et al. 2017; Tedstone et al. 2017; Williamson et al. 2018) GrIS. The algal community on the GrIS is dominated by *Mesotaenium berggrenii*, and *Ancylonema nordenskioldii* (Yallop et al., 2012; Stibal et al., 2017; Williamson et al., 2018; Lutz et al. 2018; Williamson et al. 2019), which are collectively known as “glacier algae” to distinguish them from snow algae and sea-ice-algae. The presence of these glacier algae reduces the albedo of the ice surface, mostly due to a brown-purple purpurogallin-like pigment (Williamson et al., 2018; Stibal et al., 2017; Remias et al., 2012).

An equivalent albedo reduction due to algae has also been studied on snow. Worldwide, snow algal communities are dominated by unicellular *Chlamydomonaceae*, the most abundant of which belong to the collective taxon *Chlamydomonas nivalis* (Leya et al. 2004). These algae have been shown to be associated with low-albedo snow in Eastern Greenland (Lutz et al. 2014) and to be responsible for 17 % of snowmelt in Alaska (Ganey et al. 2017). However, for glacier algae, quantification of the biological albedo reduction, radiative forcing and melt acceleration has remained elusive due to the difficulty of separating biological from non-biological albedo-reducing processes and a lack of diagnostic biosignatures for remote-sensing. For snow, remote detection has been achieved by measuring the “uniquely biological” chlorophyll absorption feature at 680 nm (Painter et al. 2001), a broader carotenoid absorption feature (Takeuchi et al. 2006), a normalised difference spectral index (Ganey et al. 2017) and a spectral unmixing model (Huovinen et al. 2018). However, these signature spectra can be ambiguous for glacier algae due to the presence of the phenolic pigment with a broad range of absorption across the UV and VIS wavelengths that obscures features associated with other pigments in raw reflectance spectra, and is further complicated by the highly variable optics of the underlying ice and mixing of algae with other impurities.

The Dark Zone is of the order  $10^5$  km<sup>2</sup> in extent and is undergoing long-term expansion (Shimada et al., 2016; Tedstone et al., 2017). Quantifying the impact of algal colonization on the Dark Zone is therefore paramount. Upscaling of unmanned aerial vehicle (UAV) observations made in a small sector of the Dark Zone to satellite data has demonstrated that “distributed impurities” including algae exert a primary control on the surface albedo, but isolating the biological effect and upscaling to the regional scale has been prevented by a lack of spectral resolution and ground validation (Ryan et al., 2018a). Recently, Wang et al. (2018) applied the vegetation red-edge (difference in reflectance between 673 and 709 nm) to map glacier algae over the south-western GrIS using Sentinel-3 OLCI data at 300 m ground resolution. Neither of these previous studies quantified the effect of glacier algae effect on albedo or melt at the regional scale.

105 Here, we directly address these issues, resolving a major knowledge gap limiting our ability to forecast ice-  
sheet melt rates into the future. First, we use spectroscopy to quantify the effect of glacier algae on albedo  
and radiative forcing in ice. We then use a new radiative transfer model to isolate the effects of individual  
light-absorbing particles on the ice surface for the first time, enabling a comparison between local mineral  
110 dust and algae and providing the first candidate albedo parameterisation that could enable glacier algae to be  
incorporated into mass balance models. To determine spatial coverage, we apply a supervised-classification  
algorithm (random-forest) to map glacier algae in multispectral UAV and satellite data. Runoff modelling  
informed by our empirical measurements and remote-sensing observations enables us to estimate the  
biological contribution to GrIS runoff for the first time.

## 2. Field sites and Methods

### 115 2.1 Overview

In this study we present a suite of empirical, theoretical and remote-sensing data to quantify and map algal  
contributions to melting on the south-western GrIS. At our field site we paired spectral reflectance and  
albedo measurements with removal of surface ice samples for biological and mineralogical analyses in order  
120 to quantify the relationship between cell abundance and broadband and spectral albedo. The imaginary part  
of the refractive index of the local mineral dusts and the purpurogallin-type phenolic compound that  
dominates absorption in the local glacier algae were measured in the laboratory and incorporated into a new  
radiative transfer model. The albedo effects of each impurity were thus examined in isolation and compared.  
At the same time, we also undertook a sensitivity study with other bulk dust optical properties from previous  
125 literature to further test the potential role of mineral dusts in darkening the ice surface. Furthermore, by  
combining albedo measurements with incoming irradiance spectra and measurements of local melt rates, we  
estimated the radiative forcing and the proportion of melting that could be attributed to algae in areas of high  
and low algal biomass ( $H_{\text{bio}}$  and  $L_{\text{bio}}$ ). At our field site we made UAV flights with a multispectral camera in  
order to map algal coverage at high spatial resolution. We achieved this by training a random-forest (RF)  
130 algorithm on our field spectroscopy data to classify the ice surface into discrete categories including  $H_{\text{bio}}$  and  
 $L_{\text{bio}}$ . This enabled estimates of algal coverage in a 200 x 200m area at our field site. We then retrained our  
classifier for Sentinel-2 satellite imagery and used this to upscale further within the south-western region of  
the GrIS (to a 100 x 100 km Sentinel-2 tile covering our field site and UAV image area). With these  
estimates of algal coverage from our remote-sensing imagery and calculations of the proportion of melting  
135 attributed to algae from our field data, we were able to estimate runoff attributed to algae using van As et  
al.'s (2017) runoff model. The details of each stage of our methodology are provided in the following  
sections 2.2 – 2.10.

### 2.2 Field Site

140

Experiments were carried out at the Black and Bloom Project field site (67.04 N, 49.07 W, Fig 1), near the Institute for Marine and Atmospheric research Utrecht (IMAU) Automatic Weather Station 'S6' on the south-western Greenland Ice Sheet between 10 – 22<sup>nd</sup> July 2017. We established a 200 x 200 m area for UAV mapping (centred on 67° 4' 40.42" N, 49° 21' 0.50" W) where only essential access was allowed (e.g. for placing ground control points (GCPs) for georectifying our UAV images) and sample removal was prohibited. We also delineated an additional adjacent 20 x 200 m area that we referred to as the "sampling strip" in which we made spectral reflectance and albedo measurements paired with removal of samples for biological and mineralogical analyses, as detailed in the following sections. The sampling strip was subdivided into smaller subregions that were then systematically visited each day of our field season. This was necessary because ice surface samples were destructively removed for analysis and this method ensured that each area visited had not been disturbed by our presence on previous days. Some ancillary directional reflectance measurements were also made at the same field site between 15 - 25<sup>th</sup> July 2016 and appended to our training dataset for supervised classification (Section 2.8).

### 2.3 Field Spectroscopy

At each site in our sampling strip, albedo was measured using an ASD (Analytical Spectral Devices, Colorado) Field-Spec Pro 3 spectroradiometer with ASD cosine collector. The cosine collector was mounted horizontally on a 1.5 m crossbar levelled on a tripod with a height between 30 - 50 cm above the ice surface. The cosine collector was positioned over a sample surface, connected to the spectroradiometer using an ASD fibre optic, then the spectroradiometer was controlled remotely from a laptop, meaning the operators could move away from the instrument to avoid shading it. Two upwards and two downwards looking measurements were made in close succession (~ 2 minutes) to account for any change in atmospheric conditions, although the measurements presented were all made during constant conditions of clear skies at solar noon  $\pm$  2 hours. Each retrieval was the average of > 20 replicates.

Immediately after making the albedo measurements, the cosine collector was replaced with a 10 degree collimating lens, enabling a nadir-view hemispheric conical reflectance factor (HCRF) measurement to be obtained. For HCRF measurements the upwards looking measurements were replaced with HCRF measurements of a flat Spectralon<sup>®</sup> panel with the spectroradiometer in reflectance mode. This protocol was followed for every sample surface with both albedo and directional reflectance measurements taking less than 5 minutes. We closely followed the methodology described by Cook et al., (2017b). Albedo is the most appropriate measurement for determining the surface energy balance, while the HCRF is closer to the measurements made by aerial remote-sensing and less sensitive to stray light reflecting from surfaces other than the homogeneous patch directly beneath the sensor. We therefore used the albedo for energy balance calculations and the HCRF for remote sensing applications in this study.

## 175 2.4 Biological Measurements

Immediately following the albedo and HCRF measurements, ice from within the viewing area of the spectrometer was removed using a sterile blade and scooped into sterile whirlpak bags, melted in the dark and immediately fixed with 3% glutaraldehyde. The samples were then returned to the University of Bristol and University of Sheffield where microscopic analyses were undertaken. Samples were vortexed thoroughly  
180 before 20  $\mu\text{L}$  was pipetted into a Fuchs-Rosenthal haemocytometer. The haemocytometer was divided into 4 x 4 image areas. These were used to count a minimum of 300 cells to ensure adequate representation of species diversity (where possible – low abundance samples had as few as one cell per haemocytometer). The volume of each image area was used to calculate cells per mL. Biovolume was determined by measuring the long and short axes of at least ten cells from each species in each sample using the measure tool in the GNU  
185 Image Manipulation Program (GIMP). The morphology of the cells in the images was used to separate them into two species: *Mesotaenium bergrenii* and *Ancylonema nordenskioldii*. These dimensions were then used to calculate the mean volume of each species in each sample, assuming the cells to be circular cylinders (after Hillebrand, 1999 and Williamson et al., 2018). The average volume was multiplied by the number of cells for each species and then summed to provide the total biovolume for each sample.

190

## 2.5 Mineral and algal optical properties and radiative transfer modelling

A new radiative transfer package, BioSNICAR\_GO, was developed for this study and was used to predict the albedo of snow and ice surfaces with algae and mineral dusts. We made a series of major updates and  
195 adaptations to the BioSNICAR model presented by Cook et al. (2017b). The package is divided into a bio-optical scheme wherein the optical properties of light-absorbing impurities and ice crystals can be calculated using Mie scattering (for small spherical particles such as black carbon or snow) or geometrical optics (for large and/or aspherical particles such as glacier algae, larger mineral dust particles and large ice crystals) and a two-stream radiative transfer model based on SNICAR (Flanner et al. 2007) which incorporates the  
200 equations of Toon et al. (1989). A schematic of the model structure is provided in Supp. Info 1.

To incorporate glacier algae into BioSNICAR\_GO, geometrical optics was employed to determine the single scattering optical properties of the glacier algae, since they are large ( $\sim 10^3 \mu\text{m}^3$ : making Mie calculations  
impractically computationally expensive) and best approximated as circular cylinders (Hillebrand, 1999; Lee  
205 and Pilon, 2003). Our approach is adapted from the geometric optics parameterisation of van Dienenhoven (2014). The inputs to the geometric optics calculations are the cell dimensions and the complex refractive index. The imaginary part of the refractive index was calculated using a mixing model based upon Cook et al., (2017b) where the absolute mass of each pigment in the algal cells was measured in field samples. The absorption spectra for the algal pigments is provided in Fig 2A. We updated Cook et al.'s (2017b) mixing  
210 model to apply a volume-weighted average of the imaginary part of the refractive index of water and the

algal pigments so that the simulated cell looks like water at wavelengths where pigments are non-absorbing. We consider this to be more physically realistic than having cells that are completely non-absorbing at wavelengths  $> 0.75 \mu\text{m}$ , especially since a water fraction ( $X_w$ ) is used in the calculations to represent the non-pigmented cellular components of the total cell volume. This approach also prevents the refractive index from becoming infinite when the water fraction is zero, removing the constraint  $0 < X_w < 1$  from the bio-optical scheme in the original BioSNICAR model. Based upon experimental evidence in Dauchet et al (2015) for the model species *C. reinhardtii*, the real part of the refractive index has been updated from 1.5 (in Cook et al. 2017b) to 1.4. The absorption coefficients from which the imaginary refractive index is calculated are from Dauchet et al (2015) apart from the purpurogallin-type phenol whose optical properties were determined empirically (Fig 2A). The calculated optical properties were added to the lookup library for BioSNICAR\_GO for a range of cell dimensions. For the simulations presented in this study, we included two classes of glacier algae representing *Mesotenium Bergrenii* and *Ancylonema nordenskioldii* with length and diameter and also the relative abundance of each species matching the means measured in our microscopy described in Section 2.4. In simulations (Supp Info 2) we found that ice albedo was relatively insensitive to the dimensions of the cells within a realistic range of lengths and diameters. This low sensitivity to cell length and diameter is likely because all of the cells considered here are large from a radiative transfer perspective.

For mineral dusts, we took measured values for surface dust composition and particle size distribution (PSD) obtained at our field site from McCutcheon et al. (in prep: hereafter, McC). We then used complex refractive indices for the appropriate minerals obtained from the existing literature, mixed them using the Maxwell-Garnett dielectric mixing approximation according to the measured mass fractions (after converting to volumetric fractions using the mineral densities), generated the single scattering optical properties using a Mie scattering code and applied a weighted average using the PSD to obtain the bulk optical properties for the dust. Since the mineralogy of the dust varied between sites we generated three dust “scenarios”: In the low-absorption scenario (LO-DUST) all the minerals were set to the the minimum volume-fraction measured across all of McC’s samples except for quartz, which comprised the remainder; in the high-absorption scenario (HI-DUST) all the minerals were set to their maximum measured volume-fraction apart from quartz which comprised the remainder; and a mean scenario (MN\_DUST) where all the minerals were present with their volume-fractions equal to the mean across all of the field samples. The mineralogy of each of these scenarios are described in Table 1. Refractive indices were not available for all of the individual minerals present in McC’s analysis, so we represented the feldspar minerals using the refractive index for andesite (Pollack et al. 1973), all pyroxenes with the refractive index for enstatite (Jäger et al., 2003), and in the absence of a refractive index for amphibole phases we used the refractive index for the similarly green mineral olivine (OCDB, 2002). Refractive indices for all other minerals were available (Rothman et al., 1998; Roush et al., 1991; Pollack et al., 1973; Egan and Hilgeman, 1983; Nitsche and Fritz, 2004).

The ice optical properties in BioSNICAR\_GO were also calculated using a parameterisation of geometric optics adapted from van Diedenhoven et al. (2014). A geometrical optics approach to generating ice optical properties was chosen because it enables arbitrarily large ice grains with a hexagonal columnar shape to be simulated, in order to better estimate the albedo of glacier ice where grains are large and aspherical. While the real ice surface is composed of irregularly shaped and sized grains, this approach enabled us to simulate our field spectra much more accurately and circumvented the requirements that individual grains be small and spherical in the case of the Lorenz-Mie approach. The optical properties of the ice grains were modelled using refractive indices from Warren and Brandt (2008). The radiative transfer model is a two-stream model described in full in Cook et al. (2017b) and Flanner et al. (2007). For the radiative transfer modelling presented in this study, the following model parameters were used: Diffuse illumination, ice crystal side-length and diameter per vertical layer = 3, 4, 5, 8, 10 mm, layer thicknesses = 0.1, 1, 1, 1, 1 cm, underlying surface albedo = 0.15, layer densities = 500, 500, 600, 600, 600 kg m<sup>-3</sup>. These ice physical properties were chosen to reduce the absolute error between the simulated albedo for ice without any impurities ('clean ice') and our mean field-measured clean-ice spectrum.

To realistically simulate measured dust and algal mass loadings on the ice surface, we took measured values for H<sub>bio</sub> field samples. For mineral dusts we took the mean and maximum mineral mass mixing ratios from McC. They measured  $394 \pm 194 \mu\text{g}_{\text{LAP}}/\text{mL}_{\text{ice}}$  of which ~95% was inorganic, giving mean and maximum mineral dust loadings of 373 and 567  $\mu\text{g}_{\text{LAP}}/\text{mL}_{\text{ice}}$ . Assuming 1 mL of ice to weigh 0.917 g, this gives mean and maximum mass-mixing ratios of 342 and 519  $\mu\text{g}_{\text{dust}}/\text{g}_{\text{ice}}$ . For glacier algae we calculated mass-mixing ratios by taking the mean cell volume across all cells in our microscope images, converting to per-cell-mass using a constant cell density (0.87 g cm<sup>-3</sup>: Hu, 2014) and multiplying by our mean and maximum H<sub>bio</sub> cell abundance. This gave mean and maximum mass-mixing ratios of 349 and 646  $\mu\text{g}_{\text{algae}}/\text{g}_{\text{ice}}$ . We also varied the mass mixing ratios over a range of hypothetical values to study the sensitivity of ice surface albedo to dust and glacier algae. Glacier algae and each of the mineral dusts (LO\_ICE, HI\_ICE, MN\_ICE,) were added individually the upper 0.1 cm layer in mixing ratios of 10, 100, 500, 1000  $\mu\text{g}_{\text{LAP}}/\text{g}_{\text{ice}}$ , plus the mean and maximum measured mass-mixing ratios for dust and algae, to quantify their effects on the surface albedo. We also ran a sensitivity study where we repeated the simulations with two other dust types, sourced from previous literature, with contrasting mineralogies to our field site.

## 2.6 Empirical measurement of mineral dust reflectance

For two samples of local mineral dusts obtained from H<sub>bio</sub> sites, we chemically removed the organic matter and measured the PSD using scanning electron microscopy (full details in Supp Info 3). The chemical cleaning method avoided the artificial "reddening" of the mineral dust sample associated with removing organic matter by ignition. We then arranged the mineral dust samples into an optically thick layer on a microscope slide and pressed them tightly against the open aperture of a Thorlabs IS200-4 2" integrating

285 sphere to measure their reflectance. The other apertures were covered with SM05CP2C caps and the sample  
reflectance was measured using the same ASD Field Spec Pro 3 as was used for field measurements.

## 2.7 Radiative forcing and biological melt acceleration

290 The biological radiative forcing was calculated by first differencing the albedo for algal surfaces and the  
albedo for clean ice surfaces measured at our field site. This gives the difference in albedo between the clean  
and algal ice surfaces,  $\alpha_{\text{diff}}$ . The product of each  $\alpha_{\text{diff}}$  and the incoming irradiance,  $I^*$ , provided the  
instantaneous power density ( $PD_{\text{alg}}$ ) absorbed by the algae. We assume that photosynthetic processes utilise  
5% of this absorbed energy – at the upper end of a realistic range for photosynthetic microalgae  
295 (Blankenship et al. 2011; Masojidek et al. 2013). The remainder of  $PD_{\text{alg}}$  is conducted into the surrounding  
ice, giving the instantaneous radiative forcing due to algae ( $IRF_{\text{alg}}$ ). Since these cells are coloured by the  
purple purpurogallin pigment, we assume the reflective radiative forcing to be negligible, as demonstrated by  
Dial et al. (2018).  $IRF_{\text{alg}}$  was calculated at hourly intervals using incoming irradiance simulated for our field  
site using the PVSystems solar irradiance program (<https://pvlighthouse.com.au>) at 1 nm spectral resolution,  
300 following Dial et al. (2018). The radiative forcing was assumed to be constant between each one hour  
timestep, meaning the radiative forcing over one hour ( $HRF_{\text{alg}}$ ) could be calculated by multiplying  $IRF_{\text{alg}}$  by  
 $3600 \text{ s h}^{-1}$ , assuming that instantaneous radiative forcing is equal to radiative forcing per second. Daily  
radiative forcing due to algae ( $RF_{\text{alg}}$ ) was then calculated as the sum of  $HRF_{\text{alg}}$  between 0000 and 2300.

305 To calculate the algal contribution to melting ( $M_{\text{alg}}$ ),  $IRF_{\text{alg}}$  was multiplied by  $10^4$  to convert the radiative  
forcing from units of  $\text{W m}^{-2}$  to  $\text{W cm}^{-2}$  and then divided by the latent heat of fusion for melting ice ( $334 \text{ J g}^{-1}$ )  
and integrated over the entire day as described above. This provided a value for the amount of melting  
caused by the presence of algae per day assuming the cold content of the ice to be depleted. We calculated  
uncertainty by running these calculations for every possible combination of our measured algal and clean ice  
310 spectra and calculating the mean, standard error and standard deviation of the pooled results.

We corroborated these estimates using a point surface energy balance model (Brock and Arnold et al. 2000;  
Tedstone, 2019a). This model predicts melting in millimeters of water equivalent given local meteorological  
data and information about the ice surface albedo and roughness. We ran this model with the albedo set equal  
315 to the broadband albedo for each clean ice (CI), heavy biomass ( $H_{\text{bio}}$ ) and light biomass ( $L_{\text{bio}}$ ) spectrum in our  
field measurements. The hourly meteorological data for 21<sup>st</sup> July 2017 used to force the model was from a  
Delta-T GP1 automatic weather station (<https://www.delta-t.co.uk/product/ws-gp1/>) positioned at our field  
site. The difference in predicted melt between the algal surfaces and the clean ice surfaces provided the melt  
attributed to the presence of algae. As for the radiative forcing calculations, the uncertainty was calculated by  
320 running the energy balance model for every possible combination of algal and clean ice spectra and  
calculating the mean, standard error and standard deviation of the pooled results.

## 2.8 UAV and Sentinel-2 remote-sensing

325 Having quantified algal melt acceleration in localised patches using the methods described in 2.2 – 2.6, we  
then used a multispectral camera mounted to a UAV to quantify algal coverage across a 200 x 200 m area at  
our field site. This sample area was kept pristine throughout the study period to minimise artefacts of our  
presence appearing in the UAV imagery. Inside the sampling area we placed fifteen 10 x 10 cm Ground  
Control points (GCPs) whose precise location was measured using a Trimble differential GPS. At these  
330 markers we also made ground spectral measurements using an ASD-Field Spec Pro 3 immediately after each  
flight. The UAV itself was a Steadidrone Mavrik-M quadcopter onto which we integrated a MicaSense Red-  
Edge multispectral camera. The camera is sensitive in 5 discrete bands with center wavelengths 475, 560,  
668, 717 and 840 nm, with bandwidths 20, 20, 10, 10, 40 nm respectively. The horizontal field of view was  
47.2° and the focal length 5.4 mm. The camera was remotely triggered through the autopilot which was  
335 programmed along with the flight coordinates in the open-source software Mission Planner  
(<http://ardupilot.org/planner/>). Images were acquired at approximately 2 cm ground resolution with 60%  
overlap and 40% sidelap. The flights were less than 20 minutes long and at an altitude of 30 m above the ice  
surface.

340 We applied radiometric calibration and geometric distortion correction procedures to acquired imagery  
following MicaSense procedures (Micasense 2019). We then converted from radiance to reflectance using  
time-dependent regression between images of the MicaSense Calibrated Reflectance Panel acquired before  
and after each flight (i.e. a regression line was computed between the reflectance of the white reference panel  
at the start and end of the flight and used to quantify the change in irradiance during the flight). Finally, the  
345 individual reflectance-corrected images were mosaiced using AgiSoft PhotoScan following procedures  
developed by the United States Geological Survey (USGS, 2017), yielding a multi-spectral ortho-mosaic  
with 5 cm ground resolution, georectified to our GCPs. There was generally close agreement between the  
ground, UAV and satellite-derived albedo although there are some differences that we believe to be the result  
of different radiometric calibration techniques for satellite, UAV and ground measurements and the differing  
350 degrees of spatial integration have been examined in detail in Tedstone et al. (in review).

To upscale further, we used multispectral data from the Copernicus Sentinel-2 satellite. We selected the 100 x  
100 km tile covering our field site (T22WEV) on the closest cloud-free day to our UAV flight on 21<sup>st</sup> July.  
The L1C product was downloaded from SentinelHub (Sinergise, Slovenia). The L1C product was processed  
355 to L2A using the European Space Agency (ESA) Sen2Cor processor, including atmospheric correction and  
reprojection to 20 m resolution.

## 2.9 Supervised Classification Algorithms and albedo mapping

360 To map and quantify spatial coverage of algae over the ice-sheet surface we employed a supervised  
classification scheme. A RF classifier was trained on the field spectra collected on the ice surface (see section  
2.3) and then applied to multispectral images gathered by the UAV and Sentinel-2. We also included spectra  
obtained at the same field site in July 2016 to our training set, giving a total of 231 labelled spectra. A  
schematic of the classification workflow is provided in Supp Info 4. Our HCRF measurements were first  
365 reduced to reflectance values at five key wavelengths coincident with the centre wavelengths measured by  
the MicaSense Red-Edge camera mounted to the UAV (blue: 0.475, green: 0.560, red: 0.668, red-edge:  
0.717, NIR: 0.840  $\mu\text{m}$ ) yielding reflectance at each wavelength as a feature vector for the classifier. The  
classification labels were the surface type as determined by visual inspection: SN (snow), CI (clean ice), CC  
(cryoconite), WAT (water),  $L_{\text{bio}}$  (low biomass algae) and  $H_{\text{bio}}$  (high biomass algae). For the algal surface  
370 classes our visual assessment was corroborated by microscopy as described in section 2.2. This data set was  
then shuffled and split into a training set (80%) and a test set (20%). The training set was used to train three  
individual supervised classification algorithms: Naive Bayes, K-nearest neighbours (KNN) and support  
vector machine (SVM). For the SVM, the parameters C and gamma were tuned using grid search cross  
validation. Two ensemble classifiers were also trained: a voting classifier that combined the predictions of  
375 each of the three individual classifiers, and a RF algorithm. The performance of each classifier was measured  
using precision, accuracy, recall and F1 score and also by plotting the confusion matrix and normalised  
confusion matrix for each classifier. In all cases the RF outperformed the other classifiers according to all  
available metrics (Supp Info 5). The performance of the RF classifier was finally measured on the test set,  
demonstrating the algorithm's ability to generalise to unseen data outside of the training set. Overfitting is  
380 not usually associated with the RF classifier, and the strong performance on both our training and test sets  
confirms that the model generalizes well. For these reasons, we used the RF algorithm to classify our  
multispectral UAV and Sentinel-2 images. Training the classifier using data from field spectroscopy ensures  
the quality of each labelled datapoint in the training set, since our sampling areas were homogeneous and  
surface samples analysed in the laboratory, circumventing issues of spatial heterogeneity and uncertainty in  
385 labelling that could lead to ambiguity for direct labelling of aerial images. **Comparisons between the ASD  
spectra and the UAV and Sentinel-2 spectra are provided in Supp Info 6.** Simultaneously to the surface  
classification, we calculated the albedo in each UAV pixel using the narrowband to broadband conversion of  
Knap et al. (1999) applied to the reflectance at each of the five bands.

390 This protocol was repeated for Sentinel-2 imagery. Additional bands are available for use as feature vectors  
in the case of Sentinel-2. Directional reflectance data was reduced to eight bands coincident with the centre  
wavelengths measured by Sentinel-2 at 20m ground resolution (0.480, 0.560, 0.665, 0.705, 0.740, 0.788,  
0.865, 1.610  $\mu\text{m}$ ). **Training on reduced hyperspectral data has several advantages over training directly on  
aerial multispectral data:** first, the method is sensor-agnostic because the classifier can be retrained with a  
395 different selection of wavelengths for other upscaling platforms, enhancing the reuseability of the field

measurements; second, we have confidence in our labels because each sample has been laboratory analysed to confirm its composition, reducing label ambiguity; finally, the limited field of view of the field spectrometer reduces error arising from mixing of spectra from heterogeneous ice surfaces. Sentinel-2 imagery was masked using the MeASUREs Greenland Ice Mapping Project ice mask  
400 (<https://nsidc.org/data/nsidc-0714>) to eliminate non-ice areas. Pixels with more than 30% probability of being obscured by cloud were masked using the Sentinel-2 L2A cloud product generated by the Sen2Cor processor. For the calculation of albedo in each pixel, the additional bands available in the Sentinel-2 images enabled the application of Liang et al.'s (2001) narrowband to broadband conversion.

## 405 **2.10 Comparing 2016 and 2017**

In 2017, the GrIS Dark Zone had relatively small spatial extent, high albedo and short duration in comparison to the other years in the MODIS record, particularly since 2007, whereas the Dark Zone was especially dark, widespread and prolonged in 2016 (Fig 6; Tedstone et al. 2017). We therefore conducted a  
410 comparison between the algal coverage on the same dates in 2016 and 2017. First, we examined variations in the extent and duration of the Dark Zone along with snow depths and snow clearing dates for the south western ablation zone using MODIS, extending the time series of Tedstone et al. (2017). Bare ice was mapped by applying a threshold reflectance value ( $R < 0.60$  at  $0.841\text{-}0.871\ \mu\text{m}$ ) to the MOD09GA Daily Land Surface Reflectance Collection 6 product. Within the bare-ice area, dark ice was mapped using a lower  
415 reflectance threshold ( $R < 0.45$  at  $0.62\text{--}0.67\ \mu\text{m}$ ). The area of interest was the “common area” defined by Tedstone et al. (2017) bounded within the latitudinal range  $65\text{--}70^\circ\text{N}$ , and is equal to that used by Wang et al. (2018). To measure the annual dark ice extent (in  $\text{km}^2$ ) we counted the pixels that were dark for at least 5 days each year. The annual duration was defined at each pixel as the percentage of daily cloud-free observations made in each JJA period which were classified as dark. The timing of bare ice appearance was  
420 calculated from MODIS using a rolling window approach on each pixel (see Tedstone et al. 2017). The mean snow depths were extracted from outputs from the regional climate model MAR v3.8 (Fettweis et al. 2016) run at  $7.5\ \text{km}$  resolution forced by ECMWF ERA-Interim reanalysis data (Dee et al. 2011). These data enabled a comparison of the extent and timing of dark ice in 2016 and 2017.

425 To examine algal coverage in each year we identified the Sentinel-2 tile covering our field site (22WEV) on the closest cloud-free date to the UAV flight day (21<sup>st</sup> July) in each year. These were 26<sup>th</sup> July 2017 and 25<sup>th</sup> July 2016. Since we were interested in the bare-ice zone, snow covered pixels were omitted from the calculations.

## 430 **2.11 Runoff Modelling**

Runoff at the regional scale was calculated using van As et al.'s (2017) SMB model forced with local automatic weather station and MODIS albedo observations (van As et al., 2012; 2017). The model interpolates meteorological and radiative measurements from three PROMICE automatic weather stations on the K-Transect (KAN\_L, KAN\_M and KAN\_U) and bins them into 100 m elevation bands (0 to 2,000 m a.s.l.). Surface albedo is from MODIS Terra MOD10A1 albedo and is averaged into the same 100 m elevation bins. For every one-hour time step, the model iteratively solves the surface energy balance for the surface temperature. If energy components cannot be balanced due to the 0 C surface temperature limit, a surplus energy sink for melting of snow or ice is included. If surface temperature is greater than the melting point, the surplus energy is used for melting of snow or ice. When calculating turbulent heat fluxes, aerodynamic surface roughness for momentum was set to 0.02 and 1 mm for snow and ice, respectively (after van As et al. 2005; 2012; Smeets and Van den Broeke, 2008). We extrapolate modelled runoff across the south-western GrIS (65 – 70 ° N) by deriving the areas of each elevation bin using the Greenland Ice Mapping Project (GIMP) DEM (Howat et al., 2014). Total summer runoff from bare ice was calculated by summing runoff in elevation bins that had mean daily albedo of less than 0.60. Total summer runoff from dark ice only was calculated in the same way but using a 0.39 threshold. In van As et al.'s (2017) study they compared the performance of the model with independent observations and found errors to be negligible in the bare-ice zone.

To determine the algal contribution to runoff, we used Equation 1:

$$R_{\text{alg}} = R_{\text{tot}} * ((M_{\text{Hbio}} * C_{\text{Hbio}}) + (M_{\text{Lbio}} * C_{\text{Lbio}})) \quad (\text{Eq.1})$$

where  $R_{\text{alg}}$  = Runoff due to algae,  $R_{\text{tot}}$  = the total runoff from the bare-ice zone calculated using our runoff model,  $M_{\text{Hbio}}$  and  $M_{\text{Lbio}}$  = mean percentage of total melt attributed to algae in  $H_{\text{bio}}$  and  $L_{\text{bio}}$  areas as calculated by our energy balance modelling described in section 2.6,  $C_{\text{Hbio}}$  and  $C_{\text{Lbio}}$  = the proportion of  $C_{\text{tot}}$  comprised of  $H_{\text{bio}}$  and  $L_{\text{bio}}$  areas in our UAV or Sentinel-2 images. As discussed later, the Sentinel-2 algal coverage estimate is conservative because it often fails to resolve  $H_{\text{bio}}$  surfaces and therefore provides a lower bound on the runoff attributed to algae. An upper bound was therefore also calculated by assuming the spatial coverage derived from our UAV remote-sensing – which can accurately distinguish  $L_{\text{bio}}$  and  $H_{\text{bio}}$  - surfaces is representative of the south-western Dark Zone. We were thereby able to estimate upper and lower limits for the runoff attributed to algal growth on the south western ablation zone.

### 3. Results and Discussion

#### 3.1 Algae reduce ice albedo

The ice surfaces we studied were divided into four classes depending upon the algal abundance measured in the melted ice samples: High algal abundance ( $H_{\text{bio}}$ ), Low algal abundance ( $L_{\text{bio}}$ ), Clean Ice (CI) and Snow (SN). The algal abundance (cells/mL) in each class was as follows:  $H_{\text{bio}} = 2.9 \times 10^4 \pm 2.01 \times 10^4$ ,  $L_{\text{bio}} = 4.73 \times 10^3 \pm 2.57 \times 10^3$ ,  $CI = 625 \pm 381$ ,  $SN = 0 \pm 0$  (1 SD). These cell abundances were significantly different between the classes (one-way ANOVA,  $F = 10.21$ ,  $p = 3 \times 10^{-5}$ ) which Bonferroni-corrected t-tests indicated to be due to variance between all four groups. The dominant species of algae were *Mesotaenium bergrennii* and *Ancylonema nordenskioldii* (Fig 2D), confirming observations made by Stibal et al. (2017) and Williamson et al. (2018) in the same region. Their long, thin and approximately cylindrical morphology has been shown to be near-optimal for light absorption (Kirk, 1976). The albedo of the ice surface also varied significantly between the surface classes (one-way ANOVA for broadband albedo:  $F = 7.9$ ,  $p = 2.8 \times 10^{-4}$ ), again with Bonferroni-corrected t-tests showing variance between all four groups (Supp Info 7 A,B). Greater algal abundance was associated with lower albedo, with the albedo reduction concentrated in the visible wavelengths (Fig 2B) where both solar energy receipt and algal absorption peak (Cook et al., 2017b; Williamson et al., 2018), diminishing towards longer near infra-red (NIR:  $> 0.70 \mu\text{m}$ ) wavelengths where ice absorption, represented by the effective grain size, is most likely to cause albedo differences (Warren, 1982). A strong inverse correlation (Pearson's  $R = 0.75$ ,  $p = 2.74 \times 10^{-9}$ ) was observed between the natural logarithm of algal cell abundance (cells  $\text{mL}^{-1}$ ) in the surface ice samples and broadband albedo (Fig 2C). The linear regression coefficient of determination between the albedo and the natural logarithm of cell abundance was 0.57. It is unsurprising that the cell abundance does not account for all variation in albedo because there are also albedo-reducing effects related to the physical structure of the ice and presence of melt water (as demonstrated for snow by, for example, Warren, 1982). An inverse relationship was also observed between broadband albedo and biovolume (calculated as the sum of the products of the mean measured cell volumes and the cell counts for each algal species) but the coefficient of determination was lower ( $r^2 = 0.42$ ). This may well be the result of larger cells having a smaller effect on albedo than more numerous, smaller cells for a given total volume. The relationship between absorption and scattering coefficients and cell size may also not be straightforward for algal cells due to an increasingly important contribution to the cell optical properties from internal heterogeneity, organelles, cell walls and the pigment packaging effect in larger cells (Morel and Bricaud, 1981; Haardt and Maske, 1987).

The albedo of  $H_{\text{bio}}$  and  $L_{\text{bio}}$  surfaces is depressed in the visible wavelengths ( $0.40 - 0.70 \mu\text{m}$ , Fig 2B), creating a 'red-edge' spectrum commonly used in other environments as a marker for photosynthetic pigments (Seager et al., 2005) and for mapping algae over the GrIS by Wang et al. (2018). Chlorophyll-a has a specific absorption feature at  $0.68 \mu\text{m}$  which is hard to discern in the raw spectra, but clear in the derivative spectra (Fig 3A) for  $H_{\text{bio}}$  and  $L_{\text{bio}}$  but not CI and SN. This feature has previously been described as "uniquely biological" (Painter et al., 2001) and supports the hypothesis that the albedo reduction observed in these samples is primarily due to algae. Our measurements therefore strongly indicate a biological role in reducing the albedo of the GrIS surface; however to test that the lower broadband and spectral albedo observed on

505 algal surfaces is primarily due to the presence of algal cells, it was also necessary to compare the albedo-reducing effects of the algae to that of local mineral dust.

### 3.2 Algae have greater impact on albedo than mineral dust

510 Radiative transfer simulations demonstrated that, at measured mass-mixing ratios, mineral dusts have only a very small ( $<0.003$ ) albedo reducing effect at our field site on the south-western GrIS, whereas glacier algae reduce the ice albedo by up to 0.06, not accounting for indirect albedo-reducing feedbacks. The effect of adding the mean measured mass-mixing ratio of MN-DUST to the clean ice was a very small albedo reduction of 0.002 (Table 2; Fig 3B). In contrast, adding the mean measured mass-mixing ratio of glacier algae reduced the albedo by 0.03, preferentially in the short visible wavelengths similarly to our field-measured reflectance spectra (Table 2; Fig 3B). This effect was greater when the mass mixing ratio was increased to the maximum measured values ( $646 \mu\text{g}_{\text{algae}}/\text{g}_{\text{ice}}$  and  $519 \mu\text{g}_{\text{dust}}/\text{g}_{\text{ice}}$ ) which caused an albedo reduction of 0.06 for glacier algae and 0.003 for MN-DUST. Changing the proportions of the minerals in our simulated local dusts had a very small effect on the albedo reduction. At the mean measured mass-mixing ratio, HI-DUST reduced the albedo by just 0.0023 while LO-DUST reduced the albedo by 0.0016. Even with a mass-mixing ratio of  $1000 \mu\text{g}_{\text{dust}}/\text{g}_{\text{ice}}$ , the albedo reduction due to local mineral dusts was only 0.006, 0.004 and 0.005 for the HI-DUST, LO-DUST and MN-DUST, compared to 0.08 for glacier algae.

525 Across all our simulations, the broadband albedo-reducing power of glacier algae exceeded that of the local mineral dusts, often by several orders of magnitude. At field-measured mass-mixing ratios for heavily-laden  $H_{\text{bio}}$  surfaces, mineral dusts cannot account for the broadband albedo reduction observed in the field. This is consistent with the local mineralogy being dominated by weakly-absorbing minerals with small grain sizes as measured in our field sample (Fig 3C, Fig 4; Table 2). In Supp Info 8 we demonstrate that these conclusions are robust to different dust types including those with typically Saharan optical properties and dusts with varying hematite concentrations. The radiative-transfer simulations do not account for feedbacks related to grain size/shape, near-surface meltwater accumulation and the presence of other light absorbing particles such as humic substances that might modify the spectral reflectance and exacerbate the biological albedo-reduction. Furthermore, the albedo-lowering effects of both the glacier algae and mineral dusts is reduced by the low albedo of the underlying ice. In simulations using smaller diameter, higher albedo snow grains (whose optical properties were estimated using Mie theory) the albedo reduction caused by  $1000 \mu\text{g}_{\text{dust}}/\text{g}_{\text{ice}}$  of MN-DUST increased to 0.009, 0.010 and 0.012 for grains of diameter 1500, 1000 and  $500 \mu\text{m}$  respectively.

540 The small direct albedo-reducing effect from local minerals on the ice surface is seemingly in contrast to some previous studies such as Wientjes et al. (2010; 2011) and Bøggild (2010); however, we highlight that neither of the Wientjes et al. (2010; 2011) studies directly measured the surface albedo or any optical

properties of the mineral dusts retrieved from their GrIS sampling sites and only inferred mineralogical darkening from low spectral resolution MODIS data and the presence of a “wavy pattern” observed across the dark zone. We argue that while this may be indicative of geological outcropping onto the ablation zone, it does not necessarily follow that these minerals are responsible for surface darkening. In support of this, Wientjes et al. (2011) found strongly scattering and weakly absorbing quartz to be the dominant mineral in surface ice and speculated that biota may be having a darkening effect. Bøggild et al. (2010) found mineral dust to be an albedo reducer in Kronprinz Christian’s Land (80N, 24W) but this area is geologically and climatologically distinct from our field site, and their transect only spanned ~8 km from the ice-sheet margin, being an area prone to local dust deposition. Overall, our study is consistent with previous studies that have identified the local bare-ice mineral dust is hematite-poor and rich in weakly absorbing quartz and feldspar minerals (e.g. Tedesco et al. 2013). Tedesco et al. (2013) reported their dusts being “redder” than algae. However, their minerals were sourced from cryoconite, not the ice surface, where glacier algae are scarce and the biota is dominated by a rich consortium of other microbes that lack the characteristic pigmentation of glacier algae. Furthermore, Tedesco et al. (2013) reported an average of only 0.3% goethite in their Greenland cryoconite samples. This may have been present as hematite prior to their sample processing which involved heating the samples to 500 - 1000°C. This heating treatment likely oxidised Fe-bearing mineral phases, thereby artificially introducing the observed “reddening”..

While these radiative transfer simulations indicate that mineral dust is unlikely to be directly causing the albedo decline on the GrIS, they may still influence the ice albedo indirectly by acting as substrates for the formation of low-albedo microbial-mineral aggregates known as cryoconite granules, which are often found in quasi-cylindrical melt holes or scattered over ice surfaces (Wharton et al. 1985; Cook et al. 2015a) or by providing a nutrient source stimulating algal growth (Stibal et al. 2017). This is especially true because there is evidence in the previous literature that the dust present on the GrIS bare-ice surface are likely derived from a local source with no contribution from Asian dusts or volcanic ash (Wientjes et al. 2011) and that red minerals such as hematite, goethite and ilmenite are present only in very low concentrations (Wientjes et al. 2011; Tedesco et al. 2013; Sanna and Romeo, 2018) that would have a negligible effect on the ice albedo.

Therefore, we have demonstrated using empirical measurements and radiative transfer modelling that glacier algae are potent albedo reducers on the south-west Greenland Ice Sheet and mineral dusts are not. These findings are consistent with several previous studies (Stibal et al. 2017; Yallop et al. 2012) that found mineral dust to be insignificant for explaining albedo variations in the same region.

### 3.3 Indirect effects of algae

Algae predominantly reduce the ice albedo in the visible wavelengths (0.40 – 0.70  $\mu\text{m}$ ), whereas variations in the NIR result mainly from changes to ice grain radii and the presence of liquid water (Warren, 1982;

580 Green et al., 2002). Variations in the NIR albedo between the surface classes therefore suggest that the lower  
albedo of algal surfaces is not explained entirely by enhanced absorption due to algae, but also by the  
smoother, wetter ice surface with fewer opportunities for high-angle scattering of photons (Jonsell et al.  
2003), compared to the well-drained and porous CI surfaces. The spatial and temporal development of the  
weathering crust is therefore an important control on ice albedo (Muller and Keeler, 1969; Jonsell et al.  
2003). Algal growth is stimulated by melt, which can be enhanced by algal growth (Yallop et al., 2012;  
585 Ganey et al., 2017; Stibal et al., 2017; Cook et al., 2017a,b; Dial et al., 2018) - an example of a  
biocryomorphic process where biota alter the physical, chemical and hydrological conditions of the ice  
surface with beneficial consequences to the biota (Cook et al. 2015b).

### 3.4 Algae enhance radiative forcing and melt

590 Having determined that glacier algae reduce the ice surface albedo, we took an empirical approach to  
quantifying their impact upon energy balance following Ganey et al. (2017), which includes both direct  
albedo effects (enhanced absorption of shortwave solar radiation by the algal cells) and the indirect effects  
explained above. Integrated over the entire day, this indicated a daily mean biological radiative forcing of  
595  $116 \text{ W m}^{-2}$  and  $65 \text{ W m}^{-2}$  for  $H_{\text{bio}}$  and  $L_{\text{bio}}$  surfaces respectively, similar to RFs for Alaskan snow algae  
calculated by Ganey et al (2017). We used the biological radiative forcing integrated over the entire day and  
the latent heat of fusion for ice ( $334 \text{ J cm}^{-3}$ ) to estimate  $1.35 \pm 0.01$  (S.E) cm w.e. of melting due to algae in  
 $H_{\text{bio}}$  areas on 21<sup>st</sup> July. For  $L_{\text{bio}}$  sites, biological melting on 21<sup>st</sup> July 2017 was  $1.01 \pm 0.01$  (S.E) cm w.e.

600 We corroborated this estimate using a point surface energy balance model (Brock and Arnold et al. 2000).  
The melt attributed to the presence of algae predicted by the energy balance modelling method was similar to  
that predicted using the radiative forcing method, with  $1.37 \pm 0.48$  (S.E) cm w.e. attributed to  $H_{\text{bio}}$  and  $0.95 \pm$   
 $0.41$  (S.E) cm w.e. attributed to  $L_{\text{bio}}$ . Expressing the melt attributed to algae as a proportion of the total  
melting in the algal sites gives  $26.15 \pm 3.77$  % (S.E) of the local melting attributed to algae in the  $H_{\text{bio}}$   
605 surfaces and  $21.62 \pm 5.07$  % (S.E) for  $L_{\text{bio}}$  surfaces.

### 3.5 Algae are widespread across the south-western ablation zone

Our analyses demonstrate that algae have a dramatic darkening effect on the ice surface, leading to increased  
610 melting. However, the importance of this effect depends upon the spatial extent of the algal blooms over  
thousands of kilometers. To determine spatial coverage at our field site we aclassified multispectral images  
acquired from a UAV flown over a 200 x 200 m area. The classified UAV image indicated that 78.5% of the  
area was covered by algal blooms of which 61.1% was  $L_{\text{bio}}$  and 17.4% was  $H_{\text{bio}}$  (Table 3; Fig 5). The high  
ground resolution of the imagery enabled a qualitative assessment of the algorithm performance by visual  
615 comparison between the classifier and the raw imagery (following Ryan et al. 2018a). The algorithm

produced qualitatively realistic bloom shapes, correctly placed water in channels and individual cryoconite holes in their correct positions. The confusion matrix indicates that occasional misclassifications are generally between water and cryoconite (Supp Info 9). This is unsurprising since both cryoconite and water have relatively flat spectral shapes with few spectral features and cryoconite is often found beneath pools of surface water. We also point out that our cryoconite spectral reflectance measurements were made with cryoconite filling the entire field of view of the spectrometer, so best represent large cryoconite holes or dispersed cryoconite rather than surfaces peppered with many small holes. There was also some ambiguity between thin, wet snow and bare glacier ice, as these surfaces are spectrally similar. Nevertheless, these misclassifications affect a small area of the pixel and do not affect our estimate of algal bloom coverage.

625

We also classified Sentinel-2 satellite data (Fig 5). The confusion matrices (Supp Info 9) indicate similar misclassification types and frequencies to the UAV model. The predicted algal coverage was 58.87%.  $H_{\text{bio}}$  surfaces were much less common than  $L_{\text{bio}}$  ( $H_{\text{bio}} = 2.53\%$ ,  $L_{\text{bio}} = 56.54\%$ , Table 3). The spatial coverage by algae was different in the Sentinel and UAV datasets especially for  $H_{\text{bio}}$ , likely because a) the Sentinel-2 imagery includes ice that is outside of the Dark Zone, raising the overall reflectivity, and b) even in the UAV image, which was retrieved from within the Dark Zone,  $H_{\text{bio}}$  surfaces comprise just 17% of the ice surface and have a patchy distribution. The lowest albedo surfaces – cryoconite and water – cover a small fraction (< 3%) of the total area in both UAV and Sentinel-2 images (Table 4), although we note that many individual cryoconite holes will not be detected as they are smaller than the spatial resolution of either Sentinel-2 or the UAV. The spatial coverage reported here from our multispectral UAV imagery is consistent with a k-nearest neighbours classification scheme applied to RGB (Red, Green, Blue) imagery from a fixed wing UAV flight over the Kangerlussuaq region by Ryan et al. (2018a). They found up to 85% of the ice surface to be composed of ‘ice containing uniformly distributed impurities’ in the same region of the Dark Zone in July 2014, which our observations confirm were dominated by algae. They also found < 2% of the ice surface to be cryoconite covered and water coverage was < 5% (except for a supraglacial lake in their imaged area). This analysis demonstrates that algae are a major component of the ice surface. The larger spatial coverage of algae observed in UAV images compared to Sentinel-2 images likely results from spatial integration occurring at the coarser spatial resolution associated with Sentinel-2 data, where pixels are likely to be classified as CI unless the majority of the pixel is algae-covered. Smaller  $H_{\text{bio}}$  patches are rarely detected presumably because they are unlikely to cover the majority of a 20 m pixel. The higher detection limit for algae with decreasing ground resolution makes our estimate of spatial coverage from Sentinel-2 conservative. We highlight that this will have a much larger effect on studies aiming to quantify cell abundance using Sentinel-3 where the ground resolution is 300 m.

### 650 3.6 Algae reduce the ice albedo across the south-western ablation zone

There was a significant difference between the albedos of each surface class in all four datasets, consistent with the findings from our ground spectroscopy (Table 4). The albedo of each surface class is approximately consistent between the datasets, despite the variation in spatial coverage, giving confidence in the accuracy of our remote-sensing albedo retrievals and the classification algorithm. In the expansive areas where algae are present (Fig 5) the ice albedo is on average 0.13 lower for  $L_{\text{bio}}$  and 0.25 lower for  $H_{\text{bio}}$  compared to clean ice (Table 4). This, combined with our ground-based spectroscopy, radiative forcing calculations, radiative transfer and energy balance modelling, provides robust evidence in support of algae having a significant melt-accelerating effect on the GrIS. We cannot yet explicitly separate mineral and biological effects, but our theoretical and empirical analyses indicate that: a) local mineral dust cannot explain the observed albedo reduction, b) low-albedo areas had significantly elevated algal cell numbers relative to clean ice, c) uniquely biological features were detectable in the spectra and derivative spectra for the lower albedo sites, and d) radiative transfer models incorporating algal cells with realistic pigment profiles demonstrate the mechanism of albedo reduction. These observations confirm that supervised classification of  $H_{\text{bio}}$  and  $L_{\text{bio}}$  surfaces is indeed detecting surfaces with high algal loading and can be used to estimate algal bloom extent. Again, we point out that this estimate is conservative because there is certain to be glacier algae present in low numbers in some of the areas that are classified as clean, and  $H_{\text{bio}}$  patches are often smaller than the ground resolution of Sentinel-2, raising their detection limit (Tedstone et al., in review). Furthermore, these calculations consider the total albedo-reducing effect, inclusive of ice structure and meltwater feedbacks, not only the direct light-absorbing effects of the algal biomass.

### 3.7 Algae cause enhanced GrIS runoff

We ran a surface mass balance (SMB) model forced with local automatic weather station and MODIS albedo observations (van As et al., 2012) to estimate 45.5 Gt runoff from all bare ice and 33.8 Gt from dark ice in 2017. We used the mean spatial coverage determined using our remote-sensing in each year and our radiative forcing calculations that attributed  $21.62 \pm 5.07$  (standard error) % of melting to algae in  $L_{\text{bio}}$  sites and  $26.15 \pm 3.77$  (standard error) % in  $H_{\text{bio}}$  sites to generate estimates for the GrIS runoff caused by algal growth. We have provided upper and lower estimates based on our two remote-sensing datasets, because while our UAV is able to accurately map  $H_{\text{bio}}$  and  $L_{\text{bio}}$  surfaces, we cannot be certain that the spatial coverage derived from the 200 x 200 m area is representative of the south-western Dark Zone. At the same time, our Sentinel-2 remote-sensing underestimates algal coverage because it includes ice outside of the dark zone and  $H_{\text{bio}}$  patches are often too small to be resolved at 20 m pixel resolution (Tedstone et al. in review). Therefore, we used the spatial coverage determined by our Sentinel-2 classification as a lower bound, and spatial coverage determined by our UAV classification as an upper bound on our estimate of total runoff attributed to the presence of algae.

We found that in 2017 between 4.4 – 6.0 Gt of ice loss could be attributed to the growth of algae, representing 10 - 13 % of the total runoff from the south-western GrIS, with the lower estimate generated

using algal coverage from Sentinel-2 and the upper estimate generated using spatial coverage at our field site from our UAV. When the calculations were restricted to the Dark Zone only (i.e. excluding areas in the ablation zone not classified as “dark”) algal contributions to total runoff were up to 18 %. These calculations confirm that algal growth is an important factor in the contribution of the GrIS to global sea level rise. This contribution will increase if biologically-darkened areas expand or a greater proportion of the ice is covered by high biomass blooms under warmer climates. These observations therefore indicate that the omission of biological growth is leading current models to underestimate future GrIS contributions to sea level rise.

### 3.8 Interannual variability and potential positive feedback

MODIS data (Fig 6) indicates that 2017 was a particularly high albedo year when the Dark Zone was especially small and bright, whereas 2016 was a particularly low-albedo year where the dark zone was wider and darker than most years (Fig 6 A,B and Tedstone et al. 2017). Previous field evidence (Williamson et al., 2018) demonstrates that the ice was darkened by high concentrations of algae in 2016. In our Sentinel-2 remote-sensing tile (22WEV) the bare-ice zone was wider in 2016 (6758 km<sup>2</sup>) than in 2017 (6205 km<sup>2</sup>), and a larger area was covered with algae (on 25<sup>th</sup> July 2016, 3919 km<sup>2</sup> was covered by algae compared to 3653 km<sup>2</sup> on 28<sup>th</sup> July 2017). While the proportional total algal coverage was similar between the two years (57.99 % in 2016, 58.87 % in 2017), the proportion of the algal ice that was classified H<sub>bio</sub> was much higher in 2016 (8.35 %) compared to 2017 (2.54 %). The mean albedos and their standard deviations were very similar for each ice surface class in both years (Table 4). The runoff from the south-western GrIS bare ice (albedo < 0.6) was 94.1 Gt in 2016, of which 67.6 was from dark ice (albedo < 0.39). We estimate that 8.8 – 12.2 Gt of this runoff was attributable to the growth of algae, representing 9 – 13 % of the total runoff from bare-ice sectors. The absolute values for runoff are therefore much higher but the proportion of the bare-ice total attributed to algae was approximately the same between the two years.

The snow line retreated further, earlier in 2016 compared to 2017, creating a wider bare-ice zone that existed for longer and was not transiently covered by summer snowfall events, whereas in 2017 a smaller bare-ice area was exposed later and was covered by 5 - 10 cm of snow several times during the summer (Fig 6 C, D). The more prolonged exposure of a larger bare-ice zone in 2016 enabled L<sub>bio</sub> surfaces to extend to higher elevations and biomass to accumulate to greater mass concentrations at lower elevations in summer 2016, explaining the greater H<sub>bio</sub> coverage. This indicates that the intensity of the algal bloom is a function of exposure time, as postulated by Tedstone et al. (2017) and Williamson et al. (2018). More prolonged exposure of larger ablation areas under a warming climate (Stroeve et al. 2013; Shimada et al. 2016; Tedesco et al. 2016; Tedstone et al. 2017) are likely to be prone to more spatially expansive, darker algal blooms that enhance melt rates, leading to a potential positive feedback that is not currently accounted for in surface mass balance models whereby earlier exposure of bare ice leads to enhanced algal coverage, which will be able to accumulate higher biomass, and accelerate melting. Melting, in turn stimulates algal growth by liberating nutrients and liquid water.

#### 4. Conclusions

Our measurements and modelling demonstrate that the growth of algae on the GrIS accelerates the rate of melting and increases the GrIS contribution to global sea level rise. Field spectra show a dramatic depression of the surface albedo in the visible wavelengths for surfaces contaminated by algae. Derivative analysis of the same spectra show uniquely biological absorption features and an inverse relationship was observed between biomass and surface albedo. We employ a novel radiative transfer model to show that this albedo decline cannot be attributed to local mineral dusts. Radiative forcing calculations and an energy balance model predict that melting of glacier ice can be accelerated by  $21.62 \pm 5.07$  (SE) % for  $L_{\text{bio}}$  surfaces and  $26.15 \pm 3.77$  (SE) % for  $H_{\text{bio}}$  surfaces. We demonstrate that the growth of algae occurs over a large proportion of the ablating area of the south western GrIS by identifying algal blooms in remote-sensing data from a UAV and Sentinel 2, finding 78.5 % of the surface within a 200 x 200 m sample area at our field site to be algae covered. Using Sentinel-2 we detected algae covering 57.99 % of the Kangerlussuaq region in 2017 and 58.87 % of the same region in 2016. The spatial resolution of the sensor makes these conservative estimates, especially for  $H_{\text{bio}}$  surfaces. Runoff modelling informed by our field measurements and remote-sensing estimate between 4.4 and 6.0 Gt of runoff from the south western ablation zone could be attributed to the growth of algae in summer 2017, representing 10- 13% of the total. Because 2017 was a particularly high albedo year for the south western GrIS, we also ran our analysis for the particularly low-albedo 2016 melt season. In 2016 a wider bare-ice zone was exposed for longer, and there was a concomitant increase in the extent of the algal bloom, more of which was classified as  $H_{\text{bio}}$  (high biomass). The percentage algal contribution to south western GrIS runoff was approximately the same as in 2017 (9 – 13 %) but the absolute volume was much higher (8.8 – 12.2 Gt). This interannual comparison indicates the existence of a feedback because in years where snow retreats further, earlier, there is a larger and more prolonged area for algal bloom development where melting is enhanced, stimulating further algal growth. This study therefore demonstrates that algae are important albedo-reducers and cause a melt-enhancing feedback across the south-western GrIS. The omission of these critical biological albedo feedbacks from predictive models of GrIS runoff is leading to underestimation of future ice mass loss and contribution to global sea level rise. This is particularly significant because larger ablation zones and longer growth seasons are expected in a future warmer climate.

750

#### 5 Data Availability

Codes and datasets used in this study are available at the following repositories:

755 BioSNICAR\_GO code and data: [www.github.com/jmcook1186/BioSNICAR\\_GO](https://www.github.com/jmcook1186/BioSNICAR_GO)

Ice Surface Classification codes: [www.github.com/IceSurfClassifiers](https://www.github.com/IceSurfClassifiers)

Spectra Processing codes: [www.github.com/jmcook1186/SpectraProcessing](https://www.github.com/jmcook1186/SpectraProcessing)

Field and associated data: [www.github.com/jmcook1186/Data\\_Archive\\_TC2019](https://www.github.com/jmcook1186/Data_Archive_TC2019)

## 760 **6 Author Contribution Statement**

JC developed the measurement protocol, gathered field measurements, analysed the data, wrote the main codes, curated the data repository, produced the figures and wrote the manuscript. OMcA was instrumental in building and testing the UAV. AT, CW, JMcC, SH gathered field data. CW provided advice regarding  
765 microscopy and biological sampling protocols and helped with experimental design, and also led the empirical measurements of glacier algae pigmentation and absorption coefficients. AT wrote the code for radiometric calibration of multispectral imagery from the UAV and post-processed the UAV images, derived 2016 and 2017 dark ice extent from MODIS imagery, analysed MAR snow depth outputs and produced Fig 6, translated the energy balance model into Python and made significant contributions to the manuscript  
770 writing and experimental design. JMcC and SM provided cleaned mineral dust and PSD data to feed into the radiative transfer model and JMcC provided useful discussions regarding experimental design. MS provided DISORT modelling and estimates of mineral dust refractive indices. MF helped develop the bio-optical model. RB provided advice regarding field spectroscopy and helped measure mineral dust refractive indices in the laboratory. AJH helped develop the experimental design. AH, JR and AMcG both provided advice on  
775 UAV remote-sensing. JR, DvA and AH modelled runoff from the GrIS dark zone. AD provided microscopy images from field samples. Other authors contributed to field work and/or sample preparation and commented on the style and content of the final manuscript.

## **7 Acknowledgements**

780 JC, AT, AJH, CW, AD, SH, AmcG, AA, TDLIF, EH, MY and MT acknowledge funding from UK National Environmental Research Council Large Grant NE/M021025/1 'Black and Bloom'. JC gratefully acknowledges the Rolex Awards for Enterprise, National Geographic and Microsoft ("AI for Earth") and NERC Standard Grant "MicroMelt" NE/S001034/1. LGB, JMcC and JBM acknowledge funding from the  
785 UK National Environmental Research Council Large Grant NE/M020770/1 'Black and Bloom' and LGB and SM acknowledge funding from the German Helmholtz Recruiting Initiative (award number I-044-16-01). TG acknowledges the Gino Watkins Memorial Fund and Nottingham Education Trust. Greenland Analogue Project (GAP) weather station data are made available through the Programme for Monitoring of the Greenland Ice Sheet ([www.promice.dk](http://www.promice.dk)). MAR v3.8.1 regional climate model outputs used estimate mean  
790 snow depth were provided by Xavier Fettweis. We thank Steven Warren and an anonymous reviewer for helpful comments that improved the manuscript.

## References

- Bamber, J., Westaway, R.M., Marzeion, B., Wouters, B.: The land ice contribution to sea level during the satellite era. *Environmental Research Letters*, 13 063008, doi: 10.1088/1748-9326/aac2f0, 2018.
- 795
- Benning, L. G., Anesio, A. M., Lutz, S., & Tranter, M.: Biological impact on Greenland's albedo. *Nature Geoscience*, 7 (10), 691. doi: 20.1038/ngeo2260, 2014.
- Blankenship, R.E., Tiede, D.M., Barber, J., Brudvig, G.W., Fleming, G., Ghirardi, M., Gunner, M.R., Junge, W., Kramer, D.M., Melis, A., Moore, T.A., Moser, C.C., Nocera, D.G., Nozik, A.J., Ort, D.R., Parson, W.W., Prince, R.C., Sayre, R.T.: Comparing photosynthetic and photovoltaic efficiencies and recognizing the potential for improvement. *Science*, 332: 805-809, 2011.
- 800
- Bøggild, C.E., Brandt, R.E., Brown, K.J., Warren, S.G.: The ablation zone in northeast Greenland: ice types, albedos and impurities. *Journal of Glaciology*, 56 (195): 101-113, 2010.
- 805
- Box, J. E., Fettweis, X., Stroeve, J. C., Tedesco, M., Hall, D. K., and Steffen, K.: Greenland ice sheet albedo feedback: thermodynamics and atmospheric drivers, *The Cryosphere*, 6, 821–839, doi:10.5194/tc-6-821-2012, 2012.
- 810
- Brock, B. W., Arnold, N.S.: A spreadsheet-based (Microsoft Excel) point surface energy balance model for glacier and snow melt studies. *Earth Surface Processes and Landforms*, 25(6), 649–658. doi:10.1002/1096-9837(200006)25:6<649::aid-esp97>3.0.co;2-u, 2000.
- 815
- Cook, J.M., Edwards, A., Irvine-Fynn, T.D.I., Takeuchi, N. Cryoconite: Dark biological secret of the cryosphere, *Progress in Physical Geography*, 40: 66 – 111, <https://doi.org/10.1177/0309133315616574>, 2015a.
- Cook, J.M., Edwards, A., Hubbard, A.: Biocryomorphology: Integrating Microbial Processes with Ice Surface Hydrology, Topography, and Roughness, *Frontiers in Earth Science*, 3 (78), doi: 10.3389/feart.2015.00078. 2015b.
- 820
- Cook, J. M., Hodson, A. J., Taggart, A. J., Mernild, S. H., and Tranter, M.: A predictive model for the spectral “bioalbedo” of snow, *J. Geophys. Res.-Earth Surf.*, 122, 434–454, <https://doi.org/10.1002/2016JF003932>, 2017a.
- 825

- Cook JM, Hodson AJ, Gardner AS, Flanner M, Tedstone AJ, Williamson C, Irvine-Fynn TD, Nilsson J, Bryant R, Tranter M. Quantifying bioalbedo: A new physically-based model and critique of empirical methods for characterizing biological influence on ice and snow albedo. *The Cryosphere*: 1–29. DOI: 10.5194/tc-2017-73, 2017b
- 830
- Dauchet, J., Blanco S., Cornet, J-F., Fournier, R: Calculation of radiative properties of phototrophic microorganisms. *Journal of Quantitative Spectroscopy and Radiative Transfer*, 161: 60-84, 2015.
- 835
- Dee, D.P., Uppala, S.M., Simmons, A.J., Berrisford, P., Poli, P., Kobayashi, S., Andrae, U., Balmaseda, M.A., Balsamo, G., Bauer, P., Bechtold, P., Beljaars, A.C.M., van de Berg, L., Bidlot, J., Bormann, N., Delsol, C., Dragani, R., Fuentes, M., Geer, A.J., Haimberger, L., Healy, S.B., Hersbach, H., Holm, E.V., Isaksen, I., Kallberg, P., Kohler, M., Matricardi, M., McNally, A.P., Monge-Sanz, B.M., Morcrette, J.-J., Park, B.-K., Peubey, C., de Rosnay, P., Tavolato, C., Thepaut, J.-N., Vitart, F.: The ERA-Interim reanalysis: configuration and performance of the data assimilation system. *Quarterly Journal of the Royal Meteorological Society*, 137 (656): 553-597, doi: 10.1002/qj.828, 2011.
- 840
- Dial, R., Ganey, G., Skiles, S.M.: What colour should glacier algae be? An ecological role for red carbon in the cryosphere. *FEMS Microbiology Ecology*, 94 (3): fiy2007, doi: 10.1093/femsec/fiy007, 2018.
- 845
- Egan, W.G., Hilgeman, T.W. *Optical properties of inhomogeneous materials: applications to geology, astronomy, chemistry and engineering*. Academic Press, San Diego, USA. ISBN: 0122326504. 1979.
- Enderlin, E. M., Howat, I. M., Jeong, S., Noh, M.-J., van Angelen, J. H., van den Broeke, M. R.: An improved mass budget for the Greenland ice sheet, *Geophysical Research Letters*, 41, 866–872, doi:10.1002/2013GL059010, 2014.
- 850
- Fettweis, X., Box, J. E., Agosta, C., Amory, C., Kittel, C., Gallée, H: Reconstructions of the 1900–2015 Greenland ice sheet surface mass balance using the regional climate MAR model, *The Cryosphere*, 2016, 1–32, doi:10.5194/tc-2016-268, 2016.
- 855
- Flanner, M. G., Zender, C. S., Randerson, J. T., and Rasch, P. J.: Present-day climate forcing and response from black carbon in snow, *J. Geophys. Res.*, 112, D11202, <https://doi.org/10.1029/2006JD008003>, 2007.
- 860
- Ganey, G.Q., Loso, M.G., Burgess, A.B., Dial, R.J.: The role of microbes in snowmelt and radiative forcing on an Alaskan icefield. *Nature Geoscience*, 10, 754–759. <https://doi.org/10.1038/ngeo3027>, 2017.

- Green, R. O., Dozier, J., Roberts, D., and Painter, T. H.: Spectral snow-reflectance models for grain size and liquid water fraction in melting snow for the solar reflected spectrum, *An. Glaciol.*, 34, 71–73, 2002.
- 865
- Haardt, H. and Maske, H.: Specific in vivo absorption coefficient of chlorophyll a at 675 nm, *Limnol. Oceanogr.*, 32, 608–619, 1987.
- Hanna, E., Navarro, F.J., Pattyn, F., Domingues, C.M., Fettweiss, X., Ivins, E.R., Nicholls, R.J., Ritz, C.,  
870 Smith, B., Tulaczyk, S., Whitehouse, P., Zwally, J.: Ice sheet mass balance and climate change. *Nature*, 498 (7452): 51 – 59, doi: 10.1038/nature12238, 2013.
- Hillebrand H, Dürselen C-D, Kirschtel D., Pollinger, U., Zohary, T: Biovolume calculation for pelagic and benthic microalgae. *Journal of Phycology*, 35: 403–24, 1999.
- 875
- Howat, I. M., Negrete, A. & Smith, B. E.: The Greenland Ice Mapping Project (GIMP) land classification and surface elevation data sets. *The Cryosphere*, 8, 1509–1518, 2014.
- Hu, W. (2014). Dry weight and cell density of individual algal and cyanobacterial cells for algae research and development. PhD thesis, University of Missouri-Columbia,  
880 <https://mospace.umsystem.edu/xmlui/bitstream/handle/10355/46477/research.pdf>
- Huovinen, P., Ramirez, J., Gomez, I. Remote sensing of albedo-reducing snow algae and impurities in the Maritime Antarctic. *ISPRS Journal of Photogrammetry and Remote Sensing*, 146: 507-517. 2018.
- 885
- Jäger, C., Fabian, D., Schrempel, F., Dorschner, J., Henning, T., Wesch, W. 'Structural processing of enstatite by ion bombardement', *Astron. Astrophys.* 401, 57-65, doi: 10.1051/0004-6361:20030002. 2003.
- Jonsell, U., Hock, R., Holmgren, B.: Spatial and temporal variations in albedo on Storglaciären, Sweden.  
890 *Journal of Glaciology*, 49(164), 59-68. doi:10.3189/172756503781830980, 2003.
- Kirk, J.T.O.: A theoretical analysis of the contribution of algal cells to the attenuation of light within natural waters III. Cylindrical and spheroidal cells. *New Phytologist*, 77: 341-358, 1976.
- 895 Knap, W.H.; Brock, B.W., Oerlemans, J., Willis, I.C.: Comparison of Landsat TM- derived and ground-based albedos of Haut Glacier d’Arolla, Switzerland. *Int. J. Remote Sens.*, 20, 3293–3310, 1999.

- Langen, P.L., Fauso, R.S., Vendecrux, B., Mottram, R.H., Box, J.E: Liquid water flow and retention on the Greenland Ice Sheet in the regional climate model HIRHAM5: local and large scale impacts. *Frontiers in Earth Science*, 4 (110), doi: 10.3389/feart.2016.00110, 2017.
- Lee, E., Pilon, L.: Absorption and scattering by long and randomly oriented linear chains of spheres. *Journal of the Optical Society of America*, 30 (9): 1892- 1900, 2013.
- 905 Leya, T. *Feldstudien und genetische Untersuchungen zur Kryptophilie der Schneevalgen Nordwestspitzbergens*. Shaker Verlag, Aachen, 2014.
- Liang, S.: Narrowband to broadband conversions of land surface albedo I. *Remote Sens. Environ.* 76, 213–238. [https://doi.org/10.1016/S0034-4257\(00\)00205-4](https://doi.org/10.1016/S0034-4257(00)00205-4), 2001.
- 910 Lutz, S., Anesio, A.M., Jorge Villar, S.E., Benning, L.G. Variations of algal communities cause darkening of a Greenland glacier, *FEMS Microbiology Ecology*, 89 (2): 402–414, <https://doi.org/10.1111/1574-6941.12351>, 2014.
- 915 Lutz, S., McCutcheon, J., McQuaid, J.B., Benning, L.G.: The diversity of ice algal communities on the Greenland Ice Sheet revealed by oligotyping. *Microbial Genomics*, 4: 1-10, doi: 10.1099/mgen.0.000159, 2018.
- Masojídek, J., Torzillo, G., Koblížek, M.: Photosynthesis in Microalgae. In *Handbook of Microalgal Culture* (eds A. Richmond and Q. Hu). doi:10.1002/9781118567166.ch2, 2013
- 920 Micasense, Red-Edge camera radiometric calibration model, <https://support.micasense.com/hc/en-us/articles/115000351194-RedEdge-Camera-Radiometric-Calibration-Model>, 2019
- 925 Morel, A. and Bricaud, A.: Theoretical results concerning light absorption in a discrete medium, and application to specific absorption of phytoplankton, *Deep-Sea Res.*, 28, 1375–1393, 1981
- Muller, F., Keeler, C.M.: Errors in short term ablation measurements on melting ice surfaces. *Journal of Glaciology*, 8 (52): 91-105, 1969.
- 930 Ngheim, S.V., Hall, D.K., Mote, T.L., Tedesco, M. Albert, M.R., Keegan, K., Shuman, C.A., DiGirolamo, N.E., Neumann, G.: The extreme melt across the Greenland Ice Sheet in 2012. *Geophysical Research Letters*, 39, L20502, doi: 10.1029/2012GL053611, 2012.

- 935 Nitsche, R., Fritz, T. Precise determination of the complex optical constant of mica. *Applied Optics*, 43(16), 3263. doi:10.1364/ao.43.003263. 2004.
- Noel, B., van de Berg, W.J., Machguth, H., Lhermitte, S., Howat, I., Fettweis X., Van den Broecke, M.R.: A daily, 1km resolution data set of downscaled Greenland Ice Sheet surface mass balance (1958-2015). *The Cryosphere*, 10: 2361-2377, doi: 10.5194/tc-10-2361-2016, 2016.
- 940 Nolin, A.W., Dozier, J.: A hyperspectral method for remotely sensing the grain size of snow. *Remote Sensing of Environment*, 74: 207-216, 2000.
- 945 Nordenskiöld, A. E.: Cryoconite found 1870, 19–25 July, on the inland ice, east of Auleitsivik Fjord, Disco Bay, Greenland, *Geol.Mag.*, 2, 157–162, 1875.
- OCDB: Optical Constants Database, Laboratory Astrophysics Group of the AIU Jena. Stubachtal Olivine dataset: [https://www.astro.uni-jena.de/Laboratory/OCDB/data/silicate/crystalline/oliv\\_vis.txt](https://www.astro.uni-jena.de/Laboratory/OCDB/data/silicate/crystalline/oliv_vis.txt). 2002.
- 950 Painter, T. H., Duval, B., and Thomas, W. H.: Detection and quantification of snow algae with an airborne imaging spectrometer, *Appl. Environ. Microbiol.*, 67, 5267–5272, <https://doi.org/10.1128/AEM.67.11.5267-5272.2001>, 2001.
- 955 Pollack, J.B., Toon, O.B., Khare, B.K. Optical properties of some terrestrial rocks and glasses. *Icarus*, 19: 372-389. 1973.
- Remias, D., Schwaiger, S., Aigner, S., Leya, T., Stuppner, H., Lutz, C.: Characterization of an UV- and VIS-absorbing, purpurogallin-derived secondary pigment new to algae and highly abundant in *Mesotaenium berggrenii* (Zygnematophyceae, Chlorophyta), an extremophyte living on glaciers, *FEMS Microbiol. Ecol.*, 960 79, 638–648, <https://doi.org/10.1111/j.1574-6941.2011.01245.x>, 2012.
- Rothman, L.S., Rinsland, C.P., Goldman, A., Massie, S.T., Edwards, D.P., Flaud, J-M., Perrin, A., Camy-Peyrey, C., Dana, V., Mandin, J.-Y., Schroeder, J., McCann, A., Gamache, R.R., Wattson, R.B., Yohino, K., Chance, K.V., Jucks, K.W., Brown, L.R., Nemtchinov, V., Varanasi, P. The HITRAN molecular spectroscopic database and HAWKS (HITRAN atmospheric workstation): 1996 edition, *Journal of Quantitative Spectroscopy and Radiative Transfer*, 60 (5): 665-710: [https://doi.org/10.1016/S0022-4073\(98\)00078-8](https://doi.org/10.1016/S0022-4073(98)00078-8), 965 1998.
- 970 Roush, T., Pollack, J., Orenberg, J. Derivation of midinfrared (5-25 $\mu$ m) optical constants of some silicates and palagonite, *Icarus*, 94: 191-208. 1991.

- 975 Rueden, C.T., Schindelin, J., Hiner, M.C., DeZonia, B.E., Walter, A.E., Arena, E.T., Eliceiri, K.W.: ImageJ2: ImageJ for the next generation of scientific image data. *BMC Bioinformatics*, 18: 529 doi: 10.1186/s12859-017-1934-z, 2017
- Ryan, J., Hubbard, A., Irvine-Fynn, T.D., Doyle, S.H., Cook, J.M., Stibal, M., Box, J.E.: How robust are in situ observations for validating satellite-derived albedo over the dark zone of the Greenland Ice Sheet? *Geophysical Research Letters*, 44 (12): 6218 – 6225, 2017.
- 980 Ryan, J., Hubbard, A., Irvine-Fynn, Cook, J., T., Smith, L.C., Cameron, K., Box, J.E.: Dark zone of the Greenland Ice Sheet controlled by distributed biologically-active impurities. *Nature Communications*, 9, 1065: doi: 10.1038/s41467-018-03353-2, 2018a.
- 985 Ryan, J., van As, D., Cooley, S.W., Cooper, M.G., Pitcher, L.H., Hubbard, A.: Greenland Ice Sheet surface melt amplified by snow line migration and bare ice exposure. *Science Advances*, 5 (3): eaav3738, doi: 10.1126/sciadv.aav3738, 2018b.
- Sanna, L., Romeo, A. Mineralogy and geochemistry of cryoconite sediments in Eqip Sermia glacier (central-west Greenland). *Journal of Mediterranean Earth Sciences*, 10: 159-166, 2018.
- 995 Seager, S., Turner, E.L., Schafer, J., Ford, E.B.: Vegetation's red edge: a possible spectroscopic biosignature of extraterrestrial plants, *Astrobiology*, 5, 372–390, 2005.
- 1000 Shepherd, A., Ivins, E. R., Barletta, V. R., Bentley, M. J., Bettadpur, S., Briggs, K. H., Bromwich, D. H., Forsberg, R., Galin, N., Horwath, M., Jacobs, S., Joughin, I., King, M. A., Lenaerts, J. T. M., Li, J., Ligtenberg, S. R. M., Luckman, A., Luthcke, S. B., McMillan, M., Meister, R., Milne, G., Mouginot, J., Muir, A., Nicolas, J. P., Paden, J., Payne, A. J., Pritchard, H., Rignot, E., Rott, H., Sohn, H.G. Rensen, L. S., Scambos, T. A., Scheuchl, B., Schrama, E. J. O., Smith, B., Sundal, A. V., van Angelen, J. H., van de Berg, W. J., van den Broeke, M. R., Vaughan, D. G., Velicogna, I., Wahr, J., Whitehouse, P. L., Wingham, D. J., Yi, D., Young, D., Zwally, H. J.: A Reconciled Estimate of Ice-Sheet Mass Balance, *Science*, 338, 1183–1189, doi:10.1126/science.1228102. 2012.
- 1005 Shimada, R., Takeuchi, N., and Aoki, T.: Inter-annual and geographical variations in the extent of bare ice and dark ice on the Greenland ice sheet derived from MODIS satellite images, *Frontiers in Earth Science*, 4, doi:10.3389/feart.2016.00043

- Skiles, S. M., Painter, T. H., Okin, G. S.: A method to retrieve the spectral complex refractive index and single scattering optical properties of dust deposited in mountain snow, *J. Glaciol.*, 63, 133–147, 1010 <https://doi.org/10.1017/jog.2016.126>, 2017.
- Smeets, C. J. P. P., Van den Broeke, M. R.: Temporal and spatial variations of the aerodynamic roughness length in the ablation zone of the Greenland ice sheet, *Bound.-Lay. Meteorol.*, 128,315–338, <https://doi.org/10.1007/s10546-008-9291-0>, 2008. 1015
- Smith, L.C., Yang, K., Pitcher, L.H., Overstreet, B.T., Chu, V.W., Rennermalm, A., Ryan, J.C., Cooper, M.G., Gleason, C.J., Tedesco, M., Jeyaratnam, J., van As, D., van den Broeke, M.R., van de Berg, W.J., Noel, B., Langen, P.L., Cullather, R.I., Zhao, B., Willis, M.J., Hubbard, A., Box, J.E., Jenner, B.A., Behar, A.E.: Direct measurements of meltwater runoff on the Greenland ice sheet surface. *PNAS*, 114 (50): E10622 – E10631, 1020 <https://doi.org/10.1073/pnas.1707743114>, 2017.
- Stibal, M., Box, J.E., Cameron, K.A., Langen, P.L., Yallop, M., Mottram, R.H., Khan, A.L., Molotch, N.P., Christmas, N.A.M., Quaglia, F.C., Remias, D., Smeets, C.J.P., van den Broeke, M.R., Ryan, J.C., Hubbard, A., Tranter, M., van As, D., Ahlstrøm, A.P.: Algae drive enhanced darkening of bare ice on the Greenland Ice 1025 Sheet. *Geophysical Research Letters*, 44 (11): 11463-11471, 2017.
- Stroeve, J., Box, J. E., Wang, Z., Schaaf, C., Baret, A.: Re-evaluation of MODIS MCD43 Greenland albedo accuracy and trends. *Remote Sensing of Environment*, 138, 99–214. doi: 10.1016/j.rse.2013.07.023, 2013.
- 1030 Takeuchi, N., Dial, R., Kohshima, S., Segawa, T., Uetake, J. Spatial distribution and abundance of red snow algae on the Harding Icefield, Alaska derived from a satellite image. *Geophysical Research Letters*, 33 (L21502), <https://doi.org/10.1029/2006GL027819>, 2006.
- Tedesco, M., Foreman, C., Anton, J., Steiner, N., Schwartzman, T.: Comparative analysis of morphological, 1035 mineralogical and spectral properties of cryoconite in Jakobshavn Isbræ, Greenland, and Canada Glacier, Antarctica. *Annals of Glaciology*, 54(63), 147-157. doi:10.3189/2013AoG63A417, 2013.
- Tedesco, M., Doherty, S., Fettweis, X., Alexander, P., Jeyaratnam, J., Nobel, E., Stroeve, J.: The darkening of the Greenland ice sheet trends, drivers and projections (1981 – 2100), *The Cryosphere*, 10, 477-496, doi: 1040 10.5194/tc-10-477-2016, 2016.
- Tedstone, A.J. Python implementation of point surface energy balance model. doi:10.5281/zenodo.3228331, 2019a.

1045

Tedstone, A.J., Bamber, J.L., Cook, J.M., Williamson, C.J., Fettweis, X., Hodson, A.J., Tranter, M.: Dark ice dynamics of the south-west Greenland Ice Sheet, *The Cryosphere Discuss*, doi: <https://www.the-cryosphere-discuss.net/tc-2017-79/>, 2017

1050

Tedstone, A. J., Cook, J. M., Williamson, C. J., Hofer, S., McCutcheon, J., Irvine-Fynn, T., Gribbin, T., and Tranter, M.: Algal growth and weathering crust structure drive variability in Greenland Ice Sheet ice albedo, *The Cryosphere Discuss.*, <https://doi.org/10.5194/tc-2019-131>, in review, 2019.

1055

Toon, O. B., McKay, C. P., Ackerman, T. P., Santhanam, K.: Rapid calculation of radiative heating rates and photodissociation rates in inhomogeneous multiple scattering atmospheres, *J. Geophys. Res.*, 94( D13), 16287– 16301, doi:10.1029/JD094iD13p16287, 1989.

1060

Uetake, J., Naganuma, T., Hebsgaard, M. B., Kanda, H., and Kohshima, S.: Communities of algae and cyanobacteria on glaciers in west Greenland, *Polar Science*, 4, 71 – 80, doi: <http://dx.doi.org/10.1016/j.polar.2010.03.002>, 2010.

United States Geological Survey (USGS), Unmanned Aircraft Systems data post-processing: Structure from motion photogrammetry, <https://uas.usgs.gov/nupo/pdf/PhotoScanProcessingMicaSenseMar2017.pdf>, 2017

1065

Van As, D., Van den Broeke, M. R., Reijmer, C. H., and Vande Wal, R. S. W.: The summer surface energy balance of the high Antarctic Plateau, *Bound. Lay. Meteorol.*, 115, 289–317, <https://doi.org/10.1007/s10546-004-4631-1>, 2005.

1070

van As, D., Hubbard, A. L., Hasholt, B., Mikkelsen, A. B., van den Broeke, M. R., Fausto, R. S.: Large surface meltwater discharge from the Kangerlussuaq sector of the Greenland ice sheet during the record-warm year 2010 explained by detailed energy balance observations, *The Cryosphere*, 6, 199-209, <https://doi.org/10.5194/tc-6-199-2012>, 2012.

1075

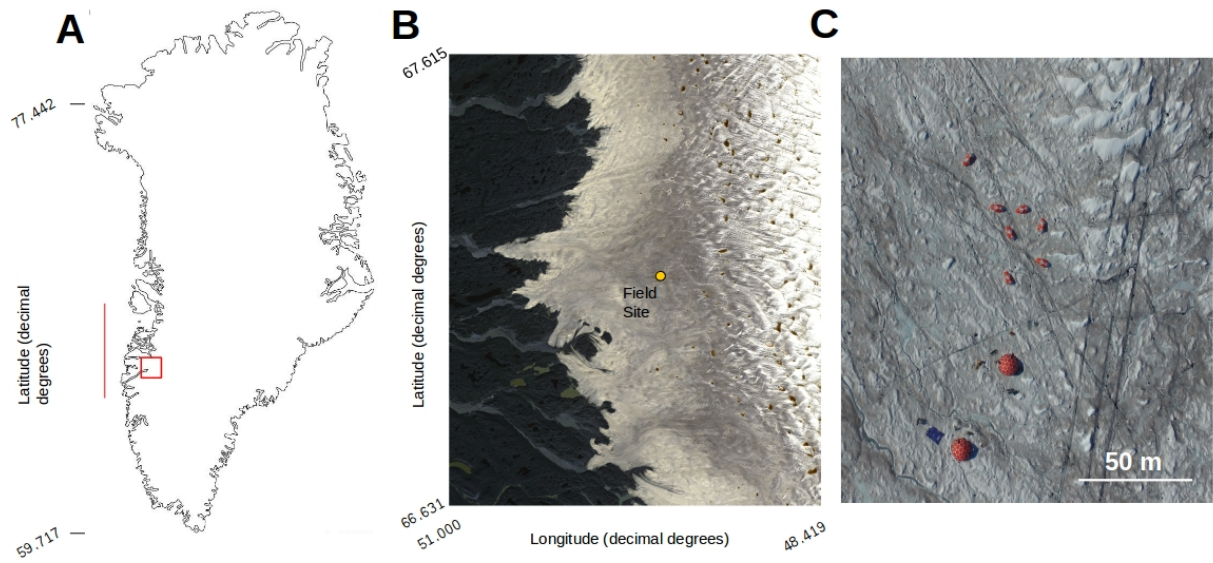
van As, D., Bech Mikkelsen, A., Holtegaard Nielsen, M., Box, J. E., Claesson Liljedahl, L., Lindbäck, K., Pitcher, L., Hasholt, B.: Hypsometric amplification and routing moderation of Greenland ice sheet meltwater release, *The Cryosphere*, 11, 1371-1386, <https://doi.org/10.5194/tc-11-1371-2017>, 2017.

1080

van den Broeke, M. R., Enderlin, E. M., Howat, I. M., Kuipers Munneke, P., Noël, B. P. Y., van de Berg, W. J., van Meijgaard, E., Wouters, B.: On the recent contribution of the Greenland ice sheet to sea level change, *The Cryosphere*, 10, 1933–1946, doi:10.5194/tc-10-1933-2016, 2016.

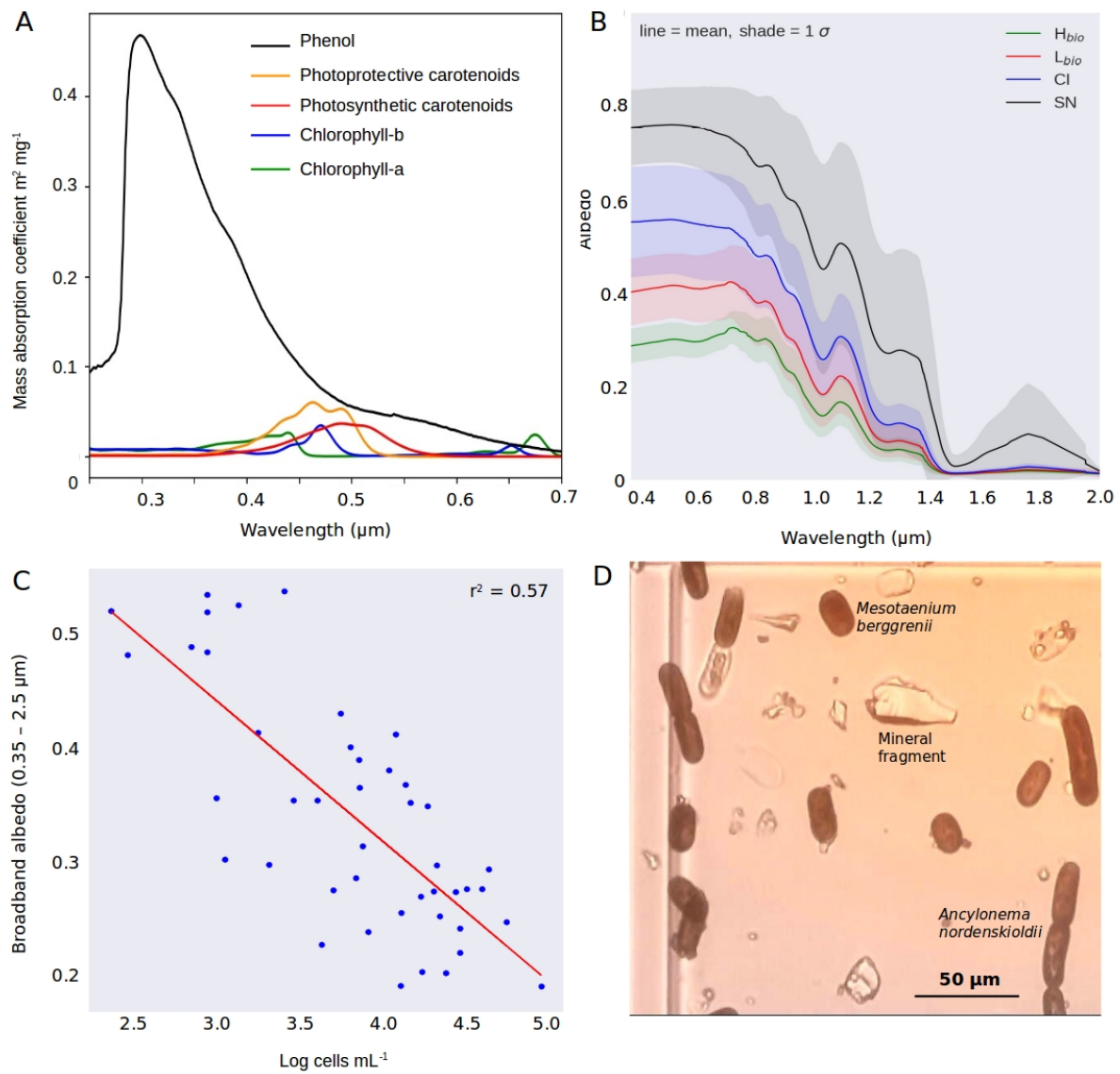
- van Dierenhoven, B., Ackerman, A.S., Cairns, B., Fridlind, A.M.: A flexible parameterization for shortwave optical properties of ice crystals. *Journal of the Atmospheric Sciences*, 71: 1763 – 1782, doi:10.1175/JAS-D-13-0205.1, 2014.
- 1085
- Wang, S., Tedesco, M., Xu, M., & Alexander, P. M. Mapping ice algal blooms in southwest Greenland from space. *Geophysical Research Letters*, 45, 11,779– 11,788. <https://doi.org/10.1029/2018GL080455>, 2018.
- Warren, S. G.: Optical properties of snow, *Rev. Geophys.*, 20, 67–89,  
1090 <https://doi.org/10.1029/RG020i001p00067>, 1982.
- Warren, S. G., Brandt, R. E.: Optical constants of ice from the ultraviolet to the microwave: A revised compilation, *J. Geophys. Res.*, 113, D14220, <https://doi.org/10.1029/2007JD009744>, 2008.
- 1095 Warren, S. G., Wiscombe, W. J.: A model for the spectral albedo of snow. 11. Snow containing atmospheric aerosols, *J. Atmos. Sci.*, 37, 2734–2745, 1980.
- Wharton, R.A., McKay, C.P., Simmons, G.M., Parker, B.C.: Cryoconite holes on glaciers. *BioScience*, 35 (8): 499-503. 1985.
- 1100
- Wientjes, I. G. M., Oerlemans, J.: An explanation for the dark region in the western melt zone of the Greenland ice sheet, *The Cryosphere*, 4, 261–268, <https://doi.org/10.5194/tc-4-261-2010>, 2010.
- Wientjes, I.G.M., Van de Wal, R.S.W., Reichert, G.J., Sluijs, A., Oerlemans, J.: Dust from the dark region in  
1105 the western ablation zone of the Greenland Ice Sheet. *The Cryosphere*, 5, 589–601, 2011, doi:10.5194/tc-5-589-2011, 2011.
- Williamson, C.J., Anesio, A.M., Cook, J., Tedstone, A., Poniecka, E., Holland, A., Fagan, D., Tranter, M., Yallop, M.L.: Ice algal bloom development on the surface of the Greenland Ice Sheet, *FEMS Microbiology Ecology*, fiy025, <https://doi.org/10.1093/femsec/fiy02>, 2018.
- 1110
- Williamson, C.J., Cameron, K.A., Cook, J.M., Zarsky, J.D., Stibal, M., Edwards, A.: Glacier Algae: A Dark Past and a Darker Future. *Front. Microbiol.* 10:524. doi: 10.3389/fmicb.2019.00524, 2019.
- 1115 Yallop, M. L., Anesio, A. J., Perkins, R. G., Cook, J., Telling, J., Fagan, D., MacFarlane, J., Stibal, M., Barker, G., Bellas, C., Hodson, A., Tranter, M., Wadham, J., and Roberts, N. W.: Photophysiology and albedo-changing potential of the ice-algal community on the surface of the Greenland ice sheet, *ISME J.*, 6, 2302–2313, 2012.

1120

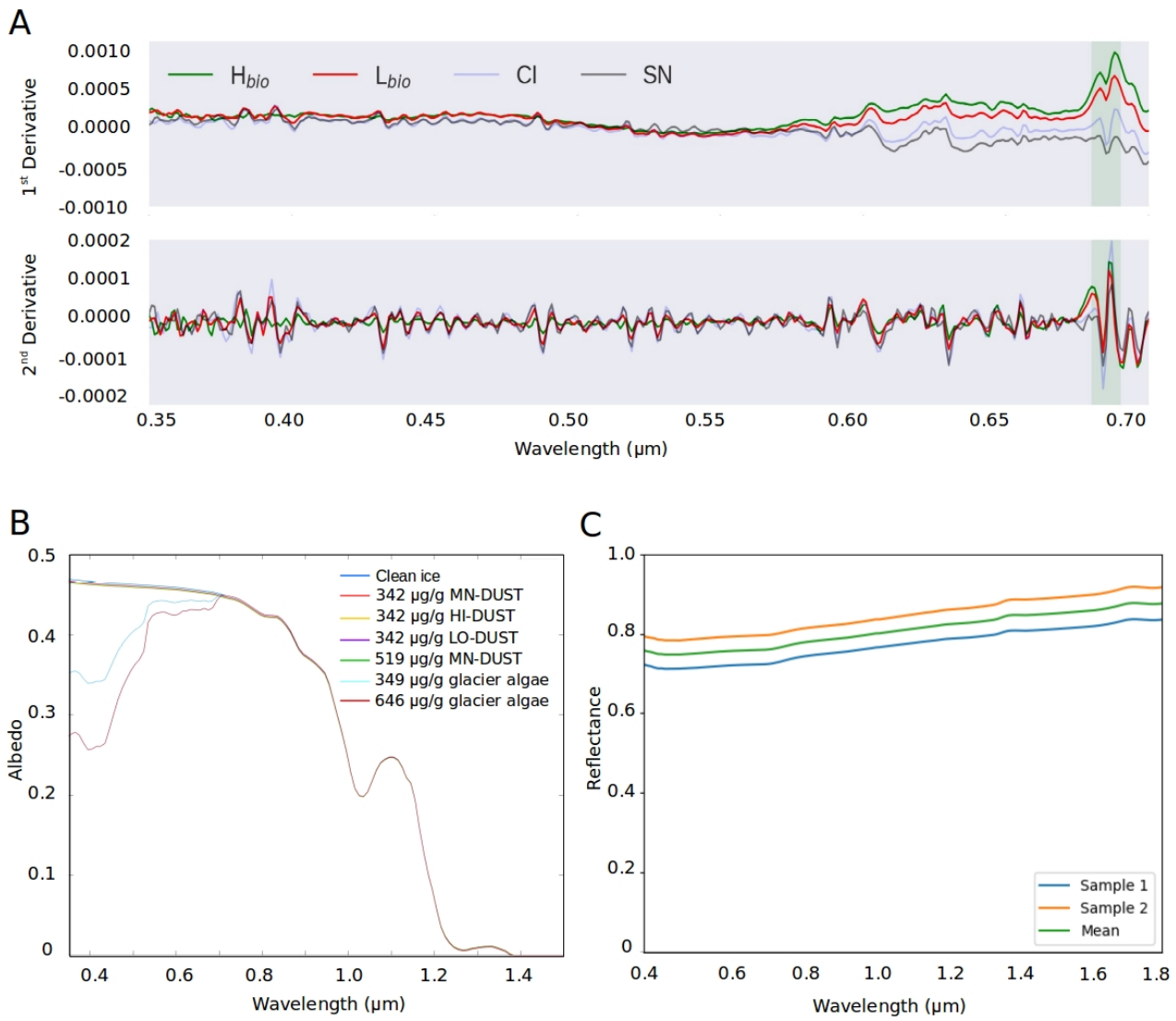


1125 Fig 1: A) Map of Greenland showing the bounding box of the Sentinel-2 tile containing our field site (red  
1130 box) and the latitudinal extent of our runoff modelling (red line). The area in the red box is presented in  
detail in B) with our field site marked with a yellow dot.

1130



1135 Fig 2 A) mass absorption coefficients of the major algal pigments including the purpurogallin-type phenol; B) Measured spectral albedos for each surface type ( $H_{\text{bio}}$  = heavy biomass loading,  $L_{\text{bio}}$  = light biomass loading, CI = clean ice, SN = snow), C) plot showing the natural logarithm of cell abundance against broadband albedo; D) microscope image showing examples of both algal species and mineral fragments from a melted  $H_{\text{bio}}$  sample.



1145 Figure 3: A) First and second derivative spectra for each surface class; B) BioSNICAR\_GO modelled  
 1146 spectral albedo for clean ice (blue) and ice with each of the simulated local dusts and algae in their measured  
 1147 mass mixing ratios in the upper 1 mm; C) Reflectance for an optically-thick layer of two samples of the local  
 1148 mineral dust.

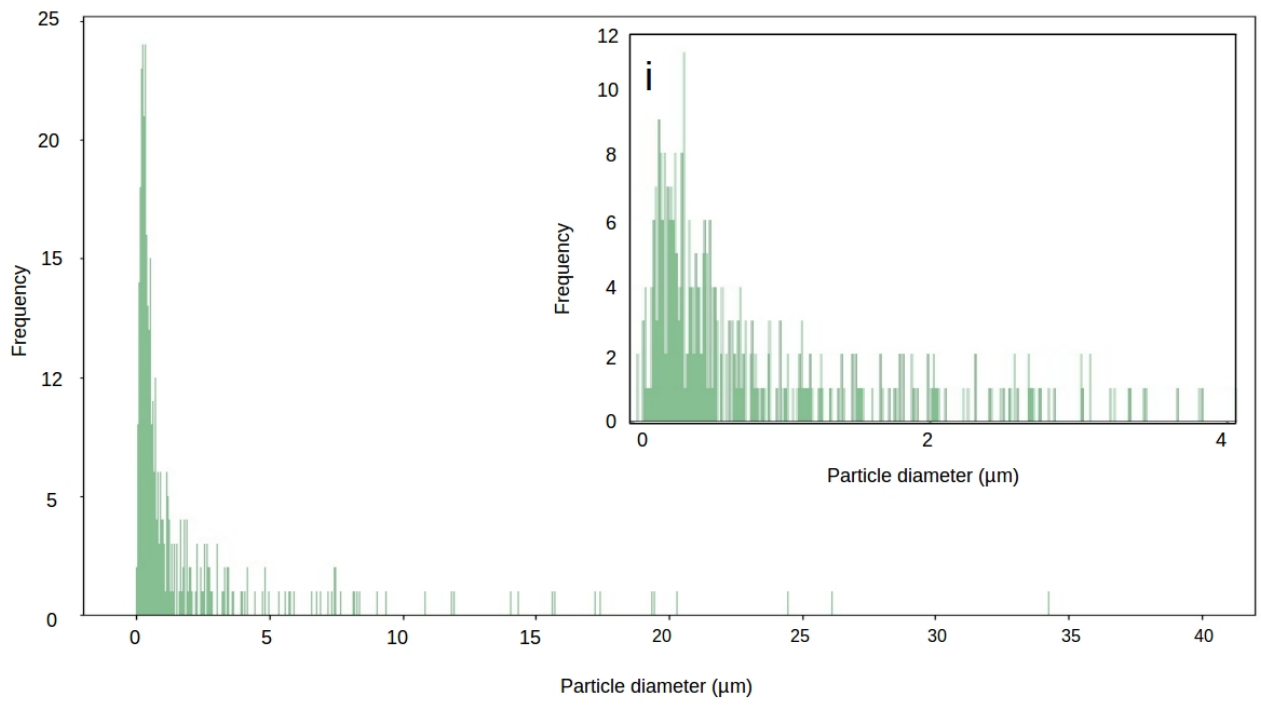
1150

1155

1160 Figure 4: Particle size diameter for our local mineral dust sample (inset i shows magnification of 0-4  $\mu\text{m}$   
 1161 range)

1160

1165



1170

1175

1180

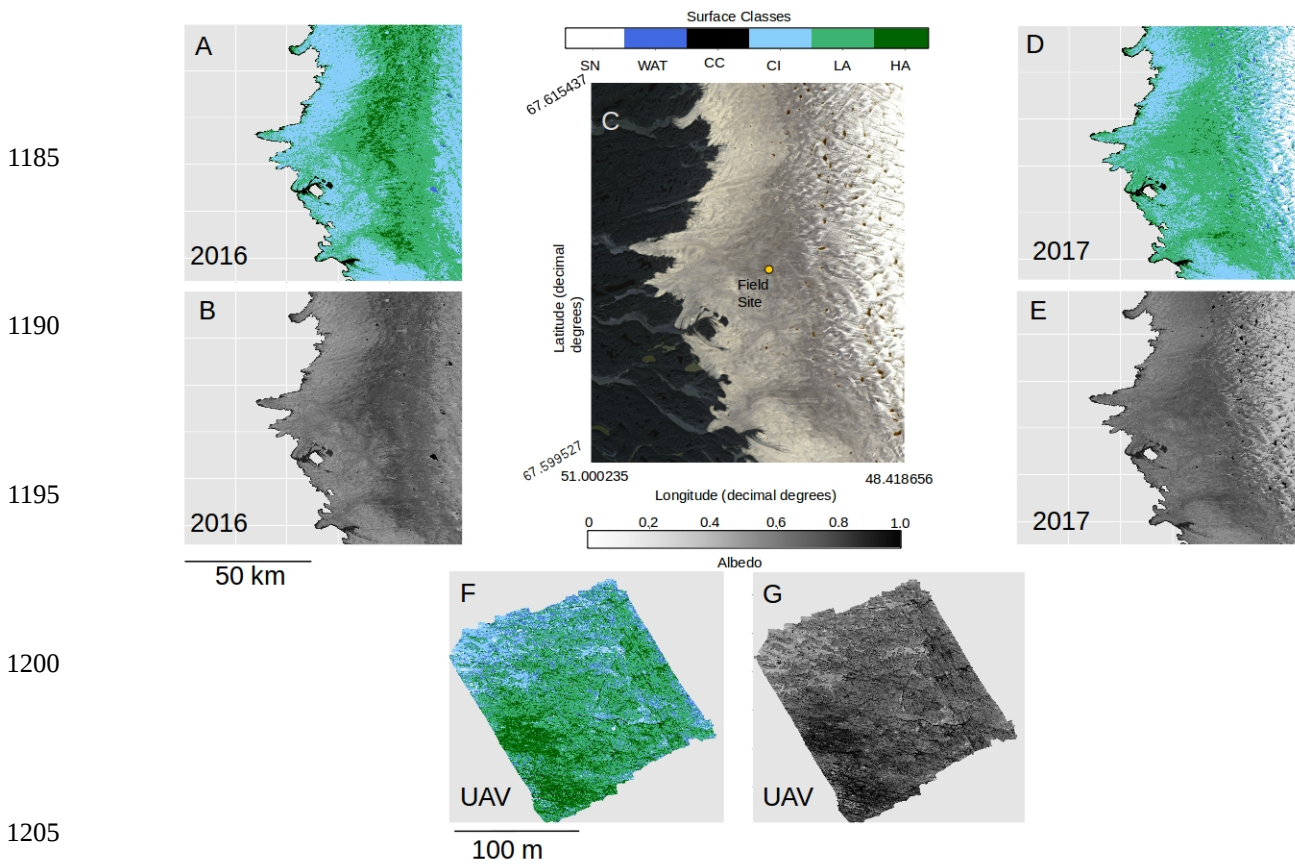
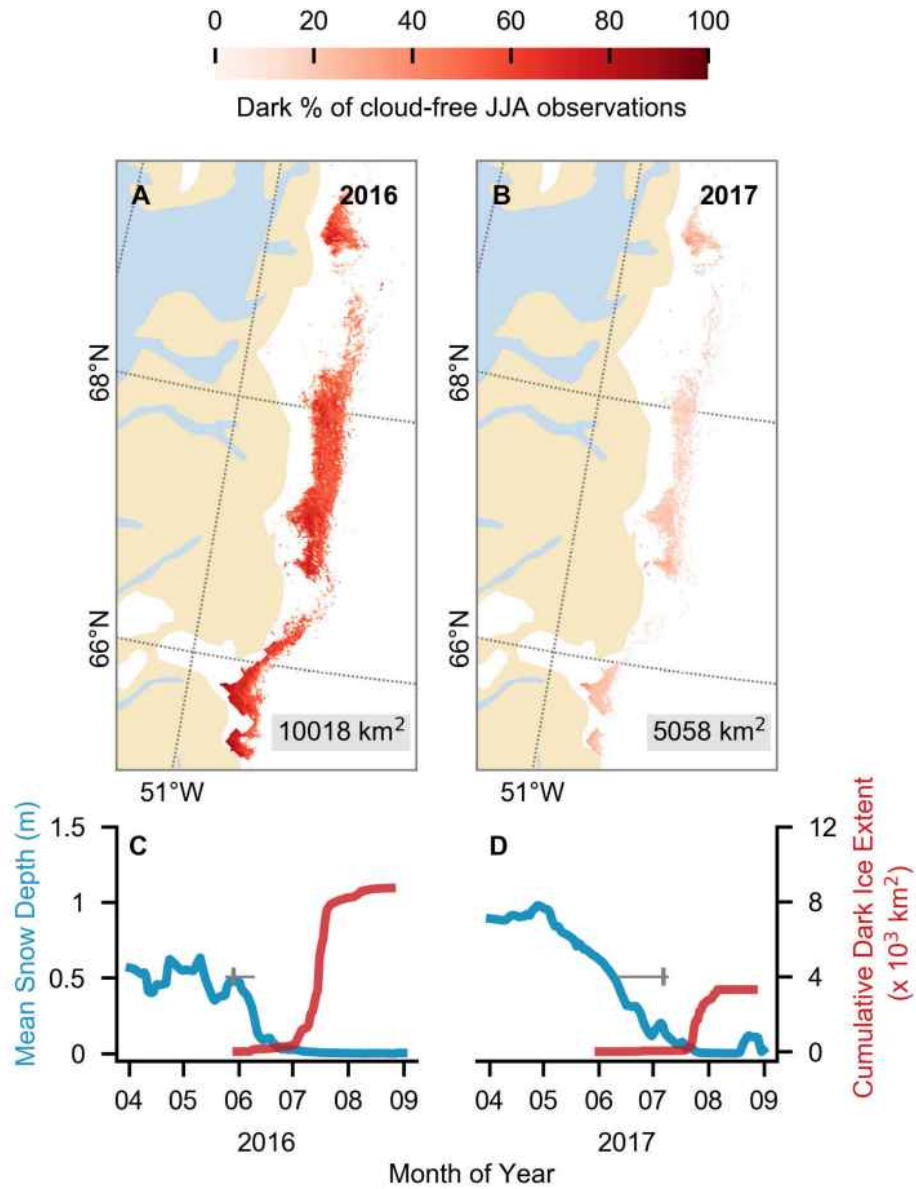


Fig 5: A) Classified map of the area shown in C for 2016. B) Broadband albedo map of the area shown in C for 2016. C) RGB “true colour” image showing the Sentinel 2 tile covering our field site in the Kangerlussuaq area. D) Classified map of the area shown in C for 2017. E) Broadband albedo map of the area shown in C for 2017. F) Classified map of a 200 x 200 m area at the field site marked in C imaged using a UAV mounted multispectral camera. G) Broadband albedo map of a 200 x 200 m area at the field site marked in C imaged using a UAV mounted multispectral camera. Panels A, B, C, D, E all use UTM Zone 22 projection and have pixel resolution of 20 m. The scale bare beneath panel B is common to panels A,B,D,E and the scale bar beneath panel F is common to panels F and G.

Figure 6: (A,B) Dark ice duration on the south-west GrIS in summers 2016 and 2017, expressed as a percentage of the total daily cloud-free observations made during June-July-August (JJA). Each year is labelled with dark ice extent. In each year, pixels that are dark for fewer than 5 days are not shown. (C,D) Average snow depth modelled by MAR (blue) and cumulative dark ice extent observed by MODIS (red) (Tedstone et al., 2017) during April to August. Vertical bars (grey) denote median date of snow clearing derived from MODIS; horizontal bars denote the interquartile range of the day of year of bare ice appearance. Tick marks denote the start of each month.



1240

Scenario	Fraction of total (% by volume)						
	Quartz	Andesite	Olivine	Enstatite	Kaolinite	Illite	Muscovite
HI-DUST	3.42	67.12	10.53	8.42	3.36	1.70	5.46
LO_DUST	45.39	50.67	3.31	0.64	0	0	0
MN_DUST	24.19	61.03	6.95	3.90	1.37	0.19	2.37

1245 Table 1: Composition of each mineral dust “scenario” in percent of total by volume.

1250

1255

1260

1265

1270

1275

1280

1285

	<b>Albedo change for various light absorbing impurity mass mixing ratios</b>								
	<b>Hypothetical mass mixing ratios (<math>\mu\text{g}_{\text{LAP}}/\text{g}_{\text{ice}}</math>)</b>					<b>Measured mass mixing ratios (<math>\mu\text{g}_{\text{LAP}}/\text{g}_{\text{ice}}</math>)</b>			
	<b>10</b>	<b>100</b>	<b>500</b>	<b>800</b>	<b>1000</b>	<b>342</b>	<b>349</b>	<b>519</b>	<b>646</b>
<b>Glacier algae</b>	-0.0010	-0.0110	-0.0460	-0.0670	-0.0800	-0.030	-0.040	-0.0487	-0.056
<b>HI-DUST</b>	-0.0001	-0.0006	-0.0030	-0.0048	-0.0060	-0.0021	-0.0023	-0.0033	-0.0039
<b>LO-DUST</b>	-0.0001	-0.0004	-0.0021	-0.0034	-0.0042	-0.0015	-0.0016	-0.0023	-0.0028
<b>MN-DUST</b>	<0.0001	<0.0001	-0.0020	-0.0043	-0.005	-0.001	-0.002	-0.0029	-0.0035

1290 Table 2: Albedo change relative to clean ice caused by the addition of each LAP to the upper 1 mm of ice in a  
range of mass mixing ratios from 10 to 1000  $\mu\text{g}_{\text{LAP}}/\text{g}_{\text{ice}}$ .

1295

1300

1305

1310

1315

1320

1325

	WAT	CC	CI	Lbio	Hbio	SN
UAV	0.31 (0.017) n = 160448	0.09 (0.031) n = 154070	0.53 (0.026) n = 2735603	0.44 (0.055) n = 12098635	0.25 (0.039) n = 3447152	0.74 (0.025) n = 63647
S2 2016	0.08 (0.044) n = 52060	0.13 (0.035) n = 272419	0.46 (0.042) n = 6771763	0.32 (0.046) n = 8388680	0.23 (0.028) n = 1410095	0.60 (0.05) n = 9924
S2 2017	0.08 (0.039) n = 174791	0.11 (0.034) n = 258520	0.46 (0.075) n = 5947314	0.31 (0.042) n = 8740186	0.22 (0.026) n = 2270206	0.76 (0.058) n = 16333853
ASD Field Spec	N/a	N/a	0.50 (0.02) n = 22	0.36 (0.07) n = 28	0.24 (0.03) n = 22	0.56 (0.10) n = 5

1330 Table 3: A) summary of the albedo for each surface class as predicted from our classified UAV image,  
Sentinel-2 image for 2016 (S2 2016) and 2017 (S2 2017) and as measured using field spectroscopy (ASD  
Field Spec) at our field site in 2017 (we do not have cosine-collector albedo measurements for water or  
cryoconite surfaces). The reported values are the mean, the standard deviation in brackets and the number of  
1335 observations.

1340

1345

1350

1355

1360

1365

	UAV Image	Sentinel 2 (2016)	Sentinel 2 (2017)
<b>Total Image Area (km<sup>2</sup>)</b>	0.04	10,000	10,000
<b>Total Algae (%)</b>	78.5	57.99	58.87
<b>H<sub>bio</sub> (%)</b>	17.4	8.35	2.54
<b>L<sub>bio</sub> (%)</b>	61.08	49.65	56.33
<b>Cryoconite (%)</b>	0.82	1.61	1.67

<b>Clean Ice (%)</b>	13.81	40.08	38.34
<b>Water (%)</b>	0.78	0.31	1.13
<b>Snow (%)</b>	6.09	n/a	n/a

1370

Table 4: percentage of each image covered by each surface type as predicted by our trained RF algorithm. Snow was removed from the calculation in the Sentinel-2 images to enable quantification of surface coverage in the bare-ice zone, i.e. below the snow line, only.

1375

1380

1385

1390

1395



Figure 1: The logo of Copernicus Publications.